

A dual-perspective evaluation framework for urban light exposure: integrating top-down visibility and bottom-up occlusion

Zhenxiang Ling^{a,b}, Xianxin Meng^{a,b}, Zihao Zheng^{a,b,c,*}, Zheng Cao^{a,**}, Zhongwen Hu^{c,d}, Benyan Jiang^e, Guanhua Guo^a, Yingbiao Chen^a, Zhifeng Wu^{a,b,c}

^a School of Geography and Remote Sensing, Guangzhou University, Guangzhou, 510006, China

^b Huangpu Research School of Guangzhou University, Guangzhou, Guangdong, 510715, China

^c MNR Key Laboratory for Geo-Environmental Monitoring of Great Bay Area, Shenzhen, 518000, China

^d School of Architecture and Urban Planning, Shenzhen University, Shenzhen, 518060, China

^e School of Architecture and Urban Planning, Guangzhou University, Guangzhou, 510006, China

ARTICLE INFO

Keywords:

SDGSAT-1

Light exposure

Population health

Visibility analysis

Dual-perspective assessment

ABSTRACT

As awareness grows about the impacts of light pollution on ecosystems and human health, regulating artificial nighttime lighting is becoming central to sustainable urban development. Street lighting is a major light source in cities and significantly affects building-level exposure. However, most studies rely on large-scale remote sensing, often oversimplifying light transmission and urban shielding, leading to biased exposure assessments. To address this gap, we propose a building-scale exposure assessment framework using the Dual-Perspective Building Light Exposure Index (DBLEI). This approach integrates denoised SDGSAT-1 imagery, street-view images, building footprints, and ground-based sky quality meter (SQM) measurements. It simultaneously considers light sources and receptors, incorporating visibility and sky view factor (SVF) analysis. Results show that (1) buildings directly facing roadways experience significantly higher light exposure than those located within urban blocks, exhibiting a distinct radial gradient from the street center; (2) exposure levels vary by street type, with Pazhou Street reaching 2,024,138.4 nW cm⁻².sr⁻¹ and Binjiang Street only 898,108.5 nW cm⁻².sr⁻¹; (3) broadband light concentrates in waterfronts and landmarks, while blue light is shaped by land use; and (4) in densely populated areas, blue light exposure shows stronger spatial coupling with population distribution. This study is among the first to quantify the contribution of street lighting to building-scale light pollution using a scalable, multi-source data framework. The findings offer valuable insights for urban lighting management, environmental planning, and public health protection.

1. Introduction

With the rapid expansion of global urbanization, population growth, and intensified economic activities, artificial lighting technologies have undergone unprecedented development, fundamentally reshaping the nocturnal light environment in cities (Cinzano et al., 2001a; Gaston et al., 2013; Longcore and Rich, 2004; Zheng et al., 2021). Urban lighting plays a vital role in ensuring nighttime traffic safety, supporting the night-time economy, and enhancing public security (Uddin and Huynh, 2017; Gaston et al., 2015; Cozens et al., 2003), and it has even become a symbol of urban culture and economic vitality (Gibson et al., 2021). However, such development is not

without cost. As cities continue to expand and population density increases, problems associated with improper lighting configuration have gradually emerged, leading to growing concerns about light pollution. It has been reported that light pollution in North America and Europe is increasing at an annual rate of approximately 6%, while densely populated regions in East Asia face even greater risks (Falchi et al., 2011). According to the *Atlas of Artificial Night Sky Brightness*, more than 80% of the global population lives under some degree of light-polluted skies; over 99% of Americans and Europeans can no longer view a pristine night sky, and more than one-third of the global population has lost visibility of the Milky Way (Falchi et al., 2016).

* Corresponding author. School of Geography and Remote Sensing, Guangzhou University, Guangzhou, 510006, China.

** Corresponding author. School of Geography and Remote Sensing, Guangzhou University, Guangzhou, 510006, China.

E-mail addresses: zhengzh@gzhu.edu.cn (Z. Zheng), jnczdl@gzhu.edu.cn (Z. Cao).

Light pollution is not merely an issue of visual overflow but poses substantial threats to both ecosystem stability and human health (Cinzano et al., 2001b). A growing body of research has demonstrated that artificial lighting disrupts natural circadian rhythms, interferes with the behavioral patterns and physiological cycles of flora and fauna, and ultimately threatens biodiversity (Boyes et al., 2021; Poot et al., 2008). In terms of human health, nighttime illumination suppresses melatonin production, disturbs sleep cycles, and is increasingly recognized as a significant risk factor for a range of health issues. Recent large-scale meta-analyses have provided robust evidence linking light at night exposure to a higher prevalence of mood disorders, including depression, bipolar disorder, and anxiety (Deprato et al., 2025). Furthermore, mechanistic studies suggest these effects are mediated through the disruption of the hypothalamic-pituitary-adrenal (HPA) axis, with adolescents being a particularly vulnerable population due to their heightened sensitivity to evening light (Guindon et al., 2024). Experimental evidence further indicates that even dim light at night can impair sleep quality and disrupt glucose and fat metabolism, leading to increased risks of chronic conditions such as obesity, diabetes, and cardiovascular diseases (Buniyaadi et al., 2025). Meanwhile, the excessive use of lighting systems leads to significant energy waste and elevated carbon emissions. It is estimated that approximately 30% of outdoor lighting in the United States is wasted, resulting in an additional 21 million tons of CO₂ emissions annually (Smith, 2009; Mizon, 2012), posing further challenges for climate change mitigation.

In response to the growing challenges posed by light pollution, the international community has begun to implement stronger regulatory and policy measures. The European Union introduced the *Eco-design Directive* to regulate the energy efficiency and light spill of outdoor lighting systems (Hölker et al., 2010), while the International Dark-Sky Association (IDA) has issued a series of technical standards to promote responsible lighting practices (Bjelajac et al., 2021). In academic research, remote sensing has emerged as a powerful tool for monitoring and evaluating urban nighttime lighting. Numerous studies have used satellite-derived nighttime light data to reveal the spatiotemporal patterns of urban illumination (Kyba et al., 2015), and applied these insights to energy modeling (Li et al., 2019) and environmental forecasting (Li et al., 2024). In recent years, the release and increasing availability of high-resolution, multispectral SDGSAT-1 imagery have opened up new possibilities for the quantitative analysis of urban lighting (Chen et al., 2024; Liu et al., 2025). However, despite these advancements, most existing remote sensing studies remain focused on the assessment of light pollution at urban or regional scales, with limited attention paid to the finer-scale lighting dynamics at the neighborhood or individual building level (Mander et al., 2023; Kyba et al., 2017; Falchi et al., 2016).

In addition to limitations in spatial scale, current mainstream studies also suffer from significant methodological constraints in their modeling perspective. Most light pollution assessments are still based on two-dimensional (2D) representations, simplifying light propagation into horizontal surface brightness distributions while neglecting the crucial influence of urban three-dimensional (3D) structures—such as building obstructions, facade orientations, and spatial density—on the pathways of light transmission (Zheng et al., 2019; Guk and Levin, 2020). In reality, however, the built environment of cities comprises highly complex geometric configurations formed by building clusters, street morphology, and topographic variation, all of which directly affect the angles of light incidence, reflection paths, and eventual exposure locations (Nasrollahi and Rostami, 2023). These 3D factors are particularly influential in high-density urban areas, where inter-building shading, facade reflectivity, and variations in visibility can significantly alter residents' perceived illumination and associated health risks. The widespread omission of such factors in existing studies introduces systematic biases in exposure estimation and hampers the precise identification of high-risk areas, thereby limiting the effectiveness of evidence-based lighting policies and interventions.

With the increasing availability of three-dimensional urban data, some studies have begun to explore the influence of built structures on light pollution exposure, particularly making initial progress on the "receptor-side" perspective. For instance, recent efforts have quantified residents' light exposure based on building-level viewsheds, offering valuable insights into fine-scale assessment (e.g., Huang et al., 2025). Nevertheless, most existing approaches still primarily focus on the emission side—measuring upward radiance or modeling ground-level luminance—while giving limited attention to how spatial configurations and urban form modulate light propagation. In particular, the shielding effects from the source side, such as occlusions caused by urban streetscapes or surrounding structures, have rarely been incorporated into exposure modeling frameworks. In complex urban environments, actual light exposure is not solely determined by the visibility from the receptor's standpoint; directional constraints and obstruction from the light source side are equally critical. Without a dual-perspective (source–receptor) modeling approach, it remains challenging to fully capture the mechanisms of light transmission from source to human targets and to accurately assess health-related exposure risks. This methodological gap is notable when contrasted with advancements in other environmental health fields. For instance, research on air pollution has progressively advanced toward high-resolution, building-scale exposure assessments. Recent studies demonstrate that three-dimensional building morphology, such as building height, significantly influences PM_{2.5} dispersion at the local neighborhood scale (Zhang et al., 2024), and mitigation strategies are increasingly focused on the building envelope itself (Perini et al., 2024). This focus on the building as a critical unit of analysis for both exposure and mitigation (Deziel et al., 2025) underscores the urgent need for a similar paradigm shift in light pollution research. Integrating such a coupled framework is essential for enabling spatially targeted strategies in urban lighting design and public health interventions.

Moreover, blue light, as the primary emission component of modern LED lighting systems, has attracted increasing attention in urban light exposure studies due to its short wavelength, high energy, and strong biological activity (Guo et al., 2023). With the widespread deployment of LED lighting in urban environments, nighttime blue light radiation has substantially increased and is considered a significant environmental factor disrupting human circadian rhythms and contributing to sleep disorders (Nagai et al., 2019). Existing studies have linked blue light exposure to sleep disturbances, alterations in body temperature, hormonal imbalances, and increased risks of cardiovascular and metabolic diseases (Heo et al., 2017; Ren et al., 2025). Some researchers have even developed melatonin suppression indices derived from blue light intensity captured by remote sensing imagery, revealing potential spatial correlations with the incidence of chronic diseases such as colorectal cancer (Aubé et al., 2013). In addition, blue light may negatively impact visual comfort and mental well-being (Lin et al., 2023). Although these studies have laid a solid foundation for understanding the physiological mechanisms of blue light effects, current research remains limited in modeling its spatial distribution and quantifying population-level exposure at the urban scale. This lack of spatial understanding hinders a comprehensive assessment of blue light pollution and constrains its integration into evidence-based public health governance and targeted intervention strategies (Huang and Chen, 2025).

To address the limitations in spatial scale, modeling perspectives, and blue light exposure quantification in existing studies, this research proposes a building-scale nighttime lighting exposure risk assessment framework. Central to this framework are two custom indices: the Dual-Perspective Building Light Exposure Index (DBLEI) and the Relative Blue Light Index (RBLI). The core logic of the DBLEI is to provide a more realistic measure of exposure by integrating two complementary viewpoints: a "top-down" perspective quantifying the visibility of celestial and ambient light sources from the building facade (the receptor side), and a "bottom-up" perspective accounting for the occlusion of ground-level light sources (e.g., streetlights) by surrounding structures like

trees and other buildings (the source side). By combining visibility and occlusion, the DBLEI moves beyond simple illuminance measurements to capture the complex modulating effects of 3D urban morphology. Furthermore, to evaluate the specific biological risks, we introduce the RBLEI. Physically, this index represents the proportion of blue light within the total nighttime light spectrum. Its scientific significance stems from the heightened sensitivity of the human circadian system to short-wavelength (blue) light, which is a potent suppressor of melatonin and has been strongly linked to health risks such as sleep disruption and mood disorders (Guindon et al., 2024). The framework is empirically applied to a typical high-density built-up area in Guangzhou, where high-resolution multispectral SDGSAT-1 satellite imagery, building footprint data, street view images, terrain information, and ground-based SQM brightness measurements are integrated to quantify light occlusion and visibility at the building level. These data serve as key inputs for modeling the dual-perspective shielding effects and visibility conditions, forming the foundation for the exposure index construction. Furthermore, the building-level exposure index is spatially coupled with high-resolution population distribution data at the neighborhood scale, enabling the identification of high-risk exposure zones and the estimation of potential health risks. Methodologically, this study achieves a transition from two-dimensional illuminance representation to three-dimensional obstruction modeling, and from physical light intensity to spatialized quantification of health-related exposure,

thereby providing a data-driven foundation and methodological pathway for refined urban lighting management and spatial public health governance.

2. Study area and data

2.1. Study area

Guangzhou, one of China's four first-tier cities, has a history of over 2200 years. It is the capital of Guangdong Province, a national central city, and a key hub for the country's economy, international trade, transportation, and scientific and technological innovation. In this study, Haizhu District and Guangzhou University Town were selected as case study areas (Fig. 1). Haizhu District is located in the central part of Guangzhou, bordered by the Pearl River to the south, and spans an area of approximately 90 km². It combines modern urban functions with ecological spaces (e.g., Haizhu Wetland Park), and is characterized by a high density of residential, commercial, and industrial buildings.

In recent years, with the rise of the nighttime economy, nighttime lighting intensity in Haizhu District has increased significantly, leading to growing concerns about light pollution. Guangzhou University Town, located in the southeast of Haizhu District, covers an area of 43 km² and hosts a cluster of universities, serving as a major educational hub in South China. The built environment is dominated by campus and

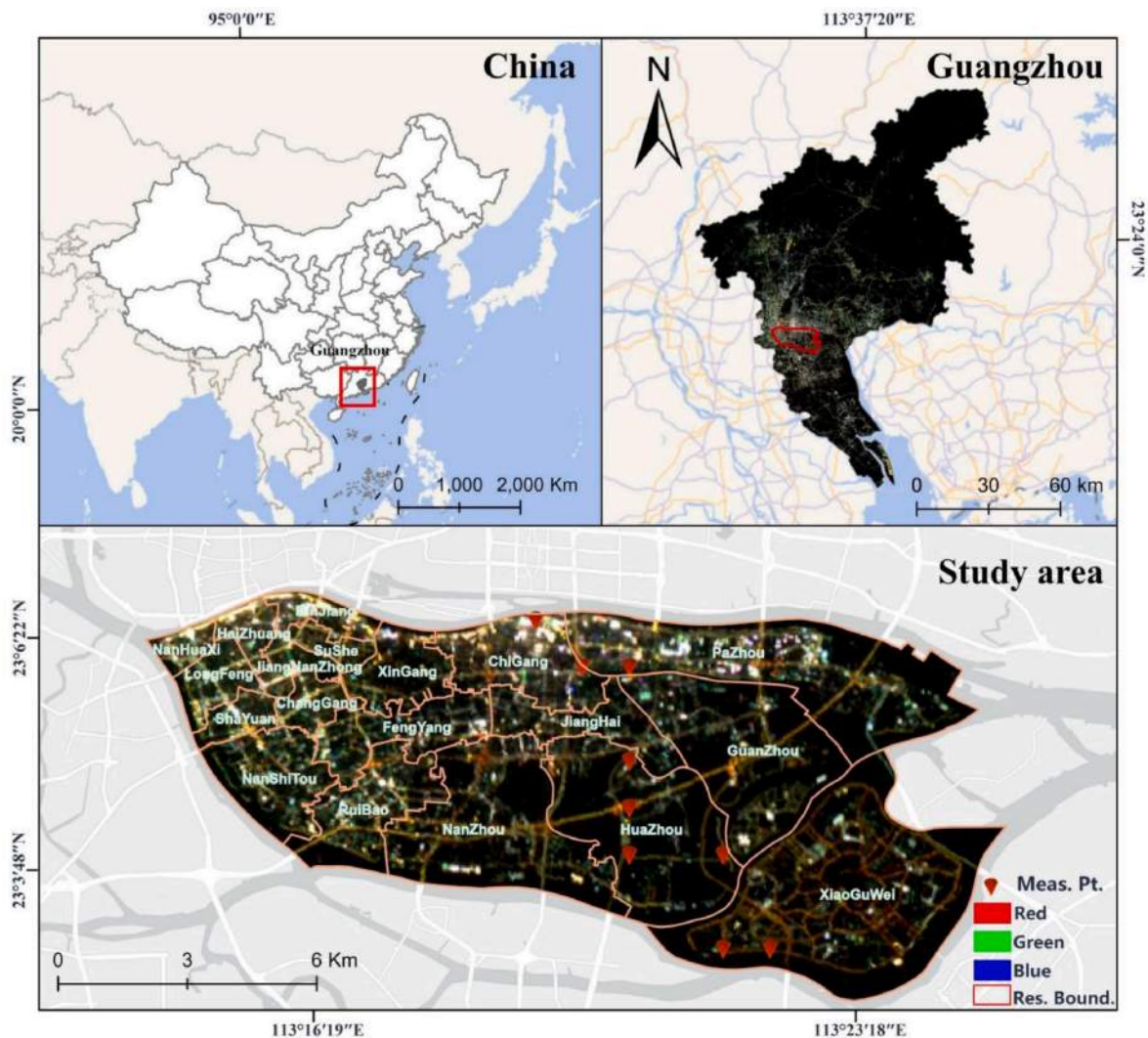


Fig. 1. Geographic location of the study area and distribution of measurement points, along with the street divisions within the study area. Note: The lower panel shows the region of interest (ROI) overlaid with RGB nightlight imagery and measurement points used for validation.

dormitory buildings, which feature large building spacing and open areas. Nighttime lighting is mainly concentrated around teaching facilities, dormitories, and public spaces, with diverse light sources and a relatively high proportion of blue light—making it a suitable site for light exposure characterization and field measurements.

2.2. Data sources and processing

This study integrates multiple heterogeneous data sources to construct a building-scale dual-perspective nighttime lighting exposure assessment framework, supporting the development of exposure indices and the spatial estimation of associated health risks. Specifically, SDGSAT-1 nighttime light imagery (at 40 m and 10 m resolution) is employed to capture the large-scale spatial distribution of nighttime light emissions. Building footprint vectors, building height data, and 30 m resolution DEM data are jointly used for receptor-side viewshed analysis, accounting for the effects of building occlusion and topographic variation on visibility.

Meanwhile, street view imagery, obtained via the Baidu Maps API and processed into image slices, is used to extract the Sky View Factor (SVF), which characterizes street-level spatial openness from the source-side perspective. Baidu heatmap data are utilized to estimate the spatial distribution of population at the neighborhood scale. After interpolation and normalization, these data reflect the intensity of human activity during nighttime across different time periods. In addition, road network data support the classification of street-scale spatial units and the selection of street-facing buildings. To evaluate the reliability of the exposure model, ground-based nighttime brightness measurements were collected using Sky Quality Meter (SQM) devices, providing validation data for assessing the consistency between modeled light intensity and actual surface brightness.

All datasets were projected and spatially aligned to ensure consistency across analysis layers. All datasets were projected and spatially aligned to ensure consistency across analysis layers. For more detailed information on the datasets and data processing procedures, please refer to Table 1 and the Methodology section.

3. Methods

3.1. Research framework

This study proposes a building-scale lighting exposure assessment framework based on a dual-perspective approach that considers both light sources and receptors. The framework primarily focuses on street-facing buildings, as they are typically located closest to major artificial light sources such as public streetlights and commercial signage, and are therefore more susceptible to nighttime light intrusion. It consists of five key components:

- (1) processing SDGSAT-1 nighttime imagery to extract high-resolution light intensity in both the panchromatic and blue spectral bands;
- (2) integrating building footprint vectors, height information, and a digital elevation model (DEM) to perform building-level viewshed analysis, quantifying receptor-side occlusion effects;

- (3) utilizing street view imagery and the derived sky view factor (SVF) to characterize spatial openness at the street scale, thereby quantifying source-side occlusion;
- (4) constructing the **Dual-Perspective Building Light Exposure Index (DBLEI)**; and
- (5) coupling the index with nighttime population distribution data derived from Baidu heatmaps to enable spatially explicit assessment of population-level exposure risk.

Fig. 2 provides an overview of the proposed methodological framework, illustrating the flow of multi-source data, key analytical procedures, and the integration logic among spatial visibility, lighting intensity, and human exposure. The subsequent sections will detail the specific methods and models applied in each step.

3.2. High-resolution nighttime illumination mapping using SDGSAT-1 data

3.2.1. Image denoising: striping and salt-and-pepper noise removal

In recent years, the availability of high-resolution multispectral nighttime remote sensing data has significantly advanced the study of urban lighting exposure. Among these data sources, SDGSAT-1, developed by the Aerospace Information Research Institute of the Chinese Academy of Sciences, provides Level-4A products with a spatial resolution of 10 m in the panchromatic band and additional multispectral channels at 40 m, including a dedicated blue-light band (<https://sdg.searh.cn/en/mobile/datas/SDGSAT>). The combination of high spatial detail and spectral specificity makes SDGSAT-1 particularly well-suited for capturing urban-scale nighttime lighting distributions. Accordingly, this study employs SDGSAT-1 nighttime imagery as the primary dataset for constructing fine-scale light intensity maps.

However, due to complex nighttime imaging conditions and sensor limitations, the original L4A images are frequently affected by various types of noise, particularly striping artifacts and salt-and-pepper noise. These issues may significantly degrade the accuracy of subsequent radiometric analyses. To improve data quality and ensure the reliability of light intensity estimation, a three-step image denoising procedure was applied as an initial preprocessing stage:

- (1) Noise Detection: Potentially corrupted pixels were identified through binarization, flagging anomalous brightness spikes and regular patterns.
- (2) Stripe Removal: Directional striping noise was detected by analyzing linear repetition in pixel values and subsequently removed using a pattern-matching and correction algorithm.
- (3) Salt-and-Pepper Filtering: A pixel-connectivity-based filtering approach was employed to eliminate isolated noisy pixels caused by sensor-level fluctuations (Zhang et al., 2022).

Finally, a 3 × 3 rectangular moving window aggregation was applied to reconstruct contaminated areas and restore spatial continuity. This process effectively enhanced the visual quality and radiometric consistency of the imagery, providing a clean input for subsequent analysis (Fig. 3).

The denoising steps described above are formalized as follows, with

Table 1
Description of the research data.

Data	Formats	Resolution	Time	Link	Application
SDGSAT-1	.tiff	10m/40 m	2024	https://www.sdgsat.ac.cn/	Nighttime light analysis
building footprint vectors	.shp		2024	https://ditu.amap.com/	Visual field and shading analysis
Street View Photo Slice	.png		2023–2024	https://map.baidu.com/	SVF
Baidu heatmap data	.shp		2024	https://map.baidu.com/	Population distribution
SQMmeasured data	.shp		2025	Field Collection	model validation
DEM	.tiff	30m	2024	https://dwtkns.com/srtm30m/	topography
Road network	.shp		2023	https://www.openstreetmap.org/	Road Network Distribution

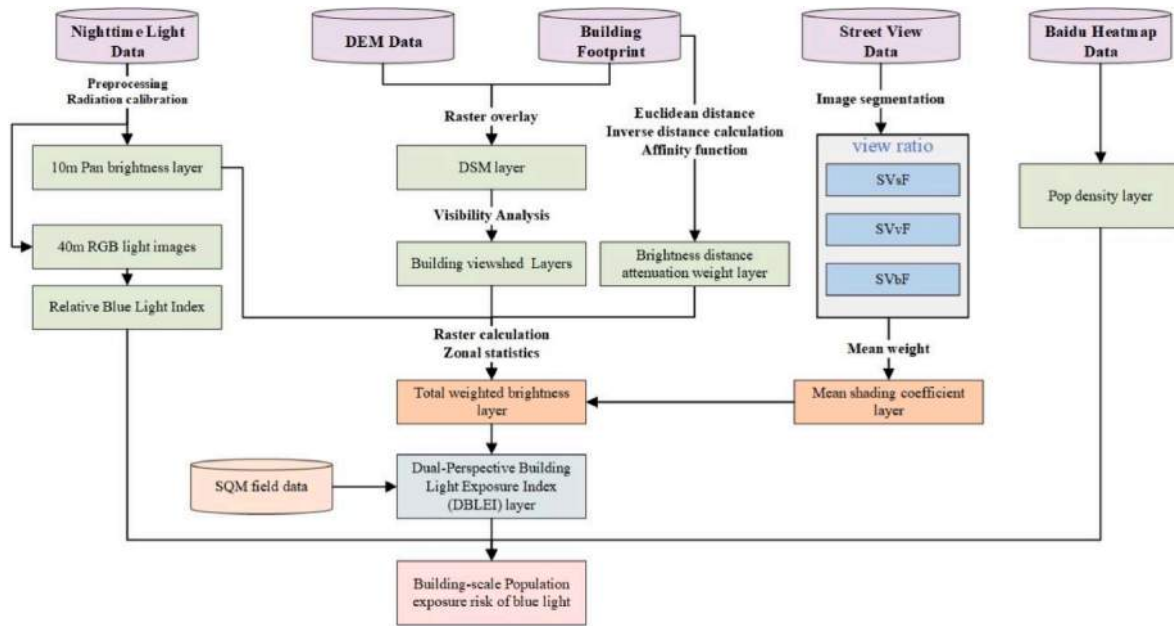


Fig. 2. Framework for dual-perspective assessment of building-level nighttime lighting and blue light exposure.

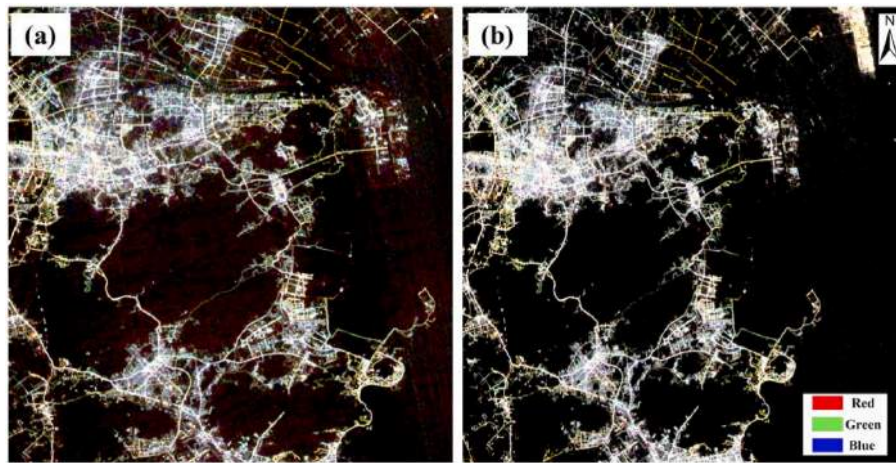


Fig. 3. An example of the SDGSAT-1 image denoising process, showing the image (a) before, and (b) after the removal of noise artifacts.

Equations (1)–(4) corresponding to noise detection, strip noise removal, pepper noise filtering, and local pixel restoration, respectively.

(1) Identification of noisy pixels via thresholding:

$$BI(i,j) = \begin{cases} 1 & \text{if } I(i,j) \geq T \\ 0 & \text{if } I(i,j) < T \end{cases} \quad (1)$$

where, $I(i,j)$ is the original pixel value at position (i,j) in the image; T is a set threshold; $BI(i,j)$ is the pixel value in the binary image, where 1 indicates a noisy pixel and 0 indicates a normal pixel.

(2) Removal of strip and pepper noise

$$I_{\text{clean}}(i,j) = I(i,j) - \text{StripNoise}(i,j) \quad (2)$$

where, $I_{\text{clean}}(i,j)$ is the pixel value of the image after removing the strip noise; $\text{StripNoise}(i,j)$ is the noise pixel detected in the direction of the strip.

$$I_{\text{filtered}}(i,j) = \text{median}(I(i,j), \{N(i,j)\}) \quad (3)$$

where, $I_{\text{filtered}}(i,j)$ is the pixel value of the image after removing the pepper noise; $N(i,j)$ is the set of neighborhood pixels around (i,j) ; median is the median filtering operation.

(3) Restoration of affected regions using local aggregation

$$I_{\text{restored}}(i,j) = \frac{1}{12} \sum_{k=0}^2 \sum_{l=0}^3 I(i+k,j+l) \quad (4)$$

where $I_{\text{restored}}(i,j)$ is the restored pixel value; $I(i+k,j+l)$ is the pixel value inside the rectangular window.

3.2.2. Radiometric calibration: conversion from DN to radiance

To convert the original digital number (DN) values of the SDGSAT-1 L4A imagery into radiance, a linear radiometric calibration model was applied following the official documentation of the satellite's data processing system (International Research Center of Big Data for SDGs, 2022). The radiance L is calculated as:

$$L = DN \times GAIN + BIAS \quad (5)$$

where L is the radiance ($\text{W}\cdot\text{m}^{-2}\cdot\text{sr}^{-1}\cdot\mu\text{m}^{-1}$), DN represents the original digital number, and $GAIN$ and $BIAS$ are calibration coefficients provided in the metadata file (.calib.xml) accompanying each L4A product.

To express the radiance in units of $\text{nW}\cdot\text{cm}^{-2}\cdot\text{sr}^{-1}$, which are commonly used in light pollution exposure assessments, a unit conversion was applied:

$$L_{SDGSAT-1} = L \times W \times 10^5 \quad (6)$$

where W denotes the spectral bandwidth. The bandwidths used in this study are 294 nm (red), 106 nm (green), 102 nm (blue), and 466 nm (panchromatic), based on instrument specifications outlined in the SDGSAT-1 User Manual (International Research Center of Big Data for SDGs, 2022).

3.2.3. Illumination mapping: generation of panchromatic and blue-band light layers

To support the building-scale assessment of nighttime lighting exposure, two illumination layers were generated from the calibrated SDGSAT-1 imagery. The first is a panchromatic light intensity layer, derived directly from the 10-m-resolution panchromatic band. This layer serves as a representation of overall nighttime brightness and is used in the exposure intensity modeling across building footprints.

The second layer focuses on the blue light component, which is of particular concern due to its short wavelength, high penetrability, and well-documented associations with circadian rhythm disruption and potential health risks. Rather than using blue-band intensity directly, we constructed an index-based representation to highlight the spectral proportion of blue light relative to total visible illumination.

The theoretical basis for this index is twofold. From a biological standpoint, the human circadian system's sensitivity is spectrally dependent, peaking in the blue-light range. Therefore, a normalized ratio quantifying the proportion of blue light is a more biologically relevant metric for health risk assessment than absolute radiance alone. From a remote sensing perspective, the use of a normalized ratio of spectral bands is a standard and widely accepted methodology for creating indices that minimize illumination variations and emphasize specific features, analogous to the well-known Normalized Difference Vegetation Index (NDVI) (Rouse Jr et al., 1973). While our RBLI is a simplified formulation adapted for multispectral satellite data, its conceptual foundation aligns with more complex, spectrally-resolved models such as the Melatonin Suppression Index (MSI) proposed by Aubé et al. (2013).

Specifically, we computed a Relative Blue Light Index (RBLI) using the radiance values of the blue (B), green (G), and red (R) bands, as follows:

$$RBLI = \frac{B}{R + G + B} \quad (7)$$

where B , G , and R represent the radiance values of the blue, green, and red bands, respectively. The RBLI layer captures spatial variations in blue light dominance, allowing us to identify high-risk zones with elevated blue light fractions even when total brightness levels are comparable. This index provides an enhanced basis for health-related exposure analysis and the spatial optimization of urban lighting systems.

3.3. Dual-perspective modeling of building-scale lighting exposure index (DBLEI)

In dense urban environments, the actual light exposure received by buildings is not solely determined by nearby light source intensity. It is also heavily influenced by the three-dimensional morphology of the built environment, including building height, spacing, and vegetative obstructions such as street trees (Nasrollahi and Rostami, 2023). However, traditional exposure assessments often rely on two-dimensional spatial models that overlook vertical occlusion and facade-specific visibility, leading to substantial inaccuracies at the building scale (Mander et al., 2023).

To address these limitations, we propose a dual-perspective modeling approach that simultaneously considers top-down source visibility and bottom-up shielding conditions. This method integrates three-dimensional building geometry, digital elevation models (DEM), and street-level visual parameters extracted from panoramic imagery via semantic segmentation. These parameters include the sky view factor (SVF), vegetation fraction, and building facade visibility, allowing for a refined estimation of actual light exposure under realistic urban occlusion conditions.

Fig. 4 presents a conceptual diagram of the proposed approach, illustrating how various urban features such as surrounding buildings and street trees interfere with the transmission of light from sources (e.g., lamps) to receptors (e.g., windows or facades).

3.3.1. Receptor-side modeling: building viewshed analysis

Most urban light pollution studies emphasize the spatial distribution and intensity of light sources, yet overlook the critical factor of whether these sources are actually visible from individual buildings. However, a

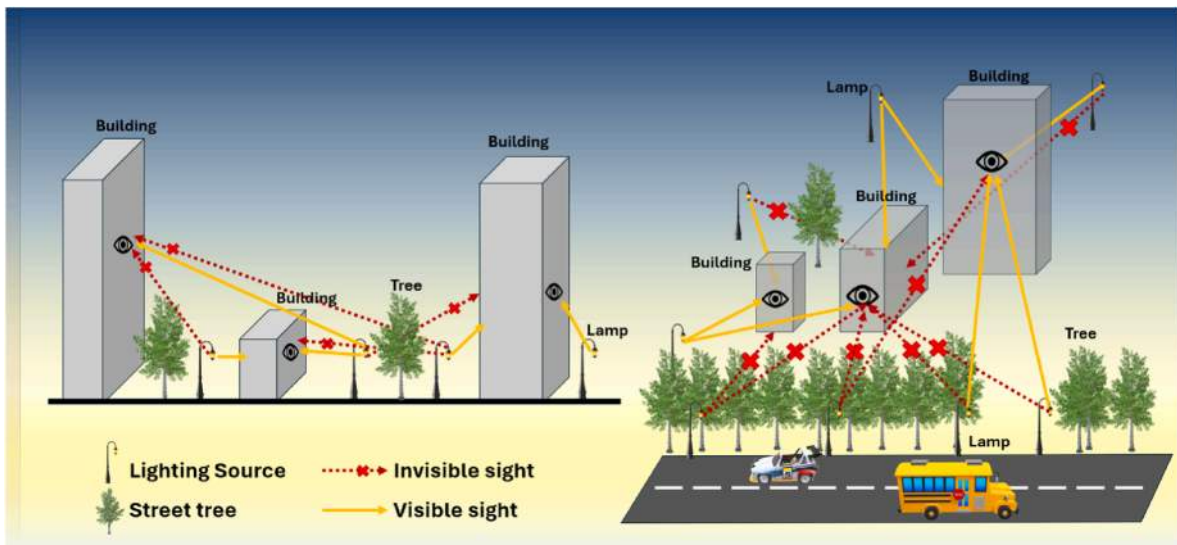


Fig. 4. Schematic diagram of visibility and occlusion modeling for building-level light exposure.

building's actual light exposure is determined not only by source intensity but also by its line-of-sight access to those sources, which is shaped by its location, orientation, and surrounding obstructions (Huang et al., 2025).

To address this gap, a building-level receptor-side visibility analysis was conducted based on viewshed modeling. The visual field of each building was simulated by incorporating building height, rooftop geometry, and surrounding urban morphology derived from the digital elevation model (DEM), enabling the estimation of its potential exposure area. This receptor-oriented modeling approach enables a more realistic quantification of light exposure at the building scale under real-world occlusion conditions, thereby correcting potential overestimations inherent in conventional models.

(1) Observation point generation

Representative observation points were generated along the external boundaries of each building to simulate light reception from the surrounding environment. To ensure geometric consistency and facade representativeness, each building footprint was first simplified using the "Minimum Bounding Geometry" tool in ArcGIS, generating a rectangle approximation. For standard rectangular buildings, four observation points were created, one along each side, with a 0.3-m outward offset applied using directional vector calculations to ensure sampling occurred outside the building envelope. These corner points were extracted using the "Feature Vertices To Points" tool, and elevation values were assigned based on 50% of the building's total height, simulating a mid-façade observation height. To avoid redundancy and ensure spatial distinctiveness, nearly overlapping or collinear points were filtered with a 0.3-m spacing threshold. This process produced a representative and reproducible set of observation points for each building, serving as the foundation for subsequent viewshed analysis.

(2) Visibility field simulation and integration

A digital surface model (DSM) was constructed to support viewshed analysis by integrating terrain elevation and building height data. Specifically, a 30-m resolution DEM (SRTM) was combined with a building height raster derived from vector building footprints. The building footprint polygons were first rasterized using ArcGIS's Polygon to Raster tool, and their height attributes were converted into a raster surface using the Raster Calculator. The resulting height raster was then added to the base DEM using Raster Math to produce a DSM that accurately reflects the built environment's vertical structure.

Using this DSM, the visibility field of each observation point was simulated. This was achieved using the `gdal.ViewshedGenerate` function from the widely-used open-source Geospatial Data Abstraction Library (GDAL), chosen for its computational efficiency and replicability. The core function of this tool is to perform a line-of-sight analysis by tracing pathways from a specified observer point to every other pixel in the digital surface model (DSM). If the path is unobstructed by the terrain or building features represented in the DSM, the target pixel is marked as visible. For each observation point, the output was a binary raster indicating visibility (1) or occlusion (0) at each pixel location. The observer height parameter was set at multiple intervals along the building facade to simulate views from different floors, providing a comprehensive, human-centric perspective on visibility.

To represent the overall visibility condition of an entire building, the individual visibility rasters of all observation points associated with that building were merged using logical union operations (i.e., pixel-wise maximum). This resulted in a composite visibility mask for each building, indicating the total area potentially visible from its facade, and serving as a spatial filter for downstream exposure estimation.

(3) Visibility-constrained light extraction

The composite visibility mask generated for each building was used to constrain the spatial scope of its light exposure assessment. Specifically, the visibility mask served as a spatial filter to extract only those pixels from the calibrated nighttime light imagery that were visible from the building's façade-level observation points. To account for the attenuation of light over distance, a distance decay weighting model was applied. This model is based on the fundamental principle that the influence of a light source diminishes as the distance from the observer increases.

First, for each building, a Euclidean distance raster was generated using ArcGIS Pro's *Euclidean Distance* tool, with the building's external observation points as the source. This raster represents the planar distance from each visible pixel to the observation surface. The inverse of this distance ($1/d_i$) was then computed and normalized to a 0–1 range to derive a continuous distance decay weight surface. The rationale for using an inverse distance function is that it provides a simple yet effective representation of light attenuation that approximates the inverse square law, a physical principle governing the propagation of light from a point source.

This weight raster was then multiplied with the calibrated nighttime radiance layer, yielding a distance-adjusted brightness surface that reflects the spatial attenuation of light. Finally, using the building's visibility mask as a binary filter, only the weighted radiance values of visible pixels were extracted and summed. The resulting visibility-constrained brightness (VCB) was defined as:

$$VCB = \sum_{i=1}^n (L_i \cdot w_i \cdot A_i) \quad (8)$$

where L_i is the radiance of the i -th visible pixel, w_i is the normalized inverse distance weight, A_i is the pixel area (typically constant) and n is the total number of pixels within the building's visible area. This distance-adjusted VCB provides a more realistic estimation of the total light energy potentially reaching a building's exterior surface. It corrects for both line-of-sight obstructions and spatial attenuation effects, thereby improving the physical fidelity of light exposure modeling in dense urban environments.

3.3.2. Source-side modeling: characterizing light source occlusion in street view

Although the preceding viewshed analysis captures visibility features from the building's perspective under 3D urban morphology and enables estimation of the light radiance each building receives within its visible domain, it does not account for smaller-scale obstructions directly in front of buildings, such as street trees, fences, or signage, which may significantly attenuate incident light. To address this limitation, we incorporated street-view imagery as a complementary data source to identify and quantify near-ground obstructions that are often invisible in elevation-based models. By performing semantic segmentation on street-level photos, we assessed the relative proportions of key occluding elements (vegetation, buildings, and sky) and examined their spatial variation across different street environments.

The source-side modeling procedure consisted of three main steps:

(1) Street view image acquisition and preprocessing

Street view images were obtained from Baidu Maps using a fixed-interval sampling strategy to ensure consistent spatial coverage of the road network. Sampling points were placed at 50-m intervals along all accessible road segments within the study area, providing dense coverage of the street environment. To ensure temporal consistency,

metadata such as image update timestamps were retrieved using the Baidu Map API, and only images captured within a defined time window were retained for further processing.

This sampling design enabled a detailed and uniform representation of urban street environments, capturing both main roads and side streets. The comprehensiveness of the sampling point distribution is illustrated in Fig. 5(a), which demonstrates the spatial extent and density of acquired images across the entire study region. These images serve as the basis for subsequent semantic segmentation and openness metric derivation.

(2) Semantic segmentation and visual composition extraction

To extract structural information relevant to light obstruction, semantic segmentation was performed on the collected street view images. Semantic segmentation is a computer vision technique that assigns a

class label (e.g., 'sky', 'vegetation', 'building') to every pixel in an image, thereby providing a detailed, pixel-level understanding of its content. For this task, we employed the DeepLabV3+ deep learning model, pre-trained on the Cityscapes dataset (Chen et al., 2018). This model was selected due to its state-of-the-art performance in accurately delineating complex urban features, which is crucial for distinguishing between light-transmitting (sky) and light-obstructing (buildings, vegetation) elements. Each image was segmented into multiple semantic categories, with particular emphasis on these three key components.

For each segmented image, the proportions of pixels corresponding to these three categories were computed, representing the visual composition of the local streetscape. These proportions reflect the degree of openness (sky fraction) and the presence of physical barriers (building and vegetation fractions) from the street-level perspective. Shadowed or visually occluded areas were implicitly captured through the absence of sky pixels or increased structural density. The resulting

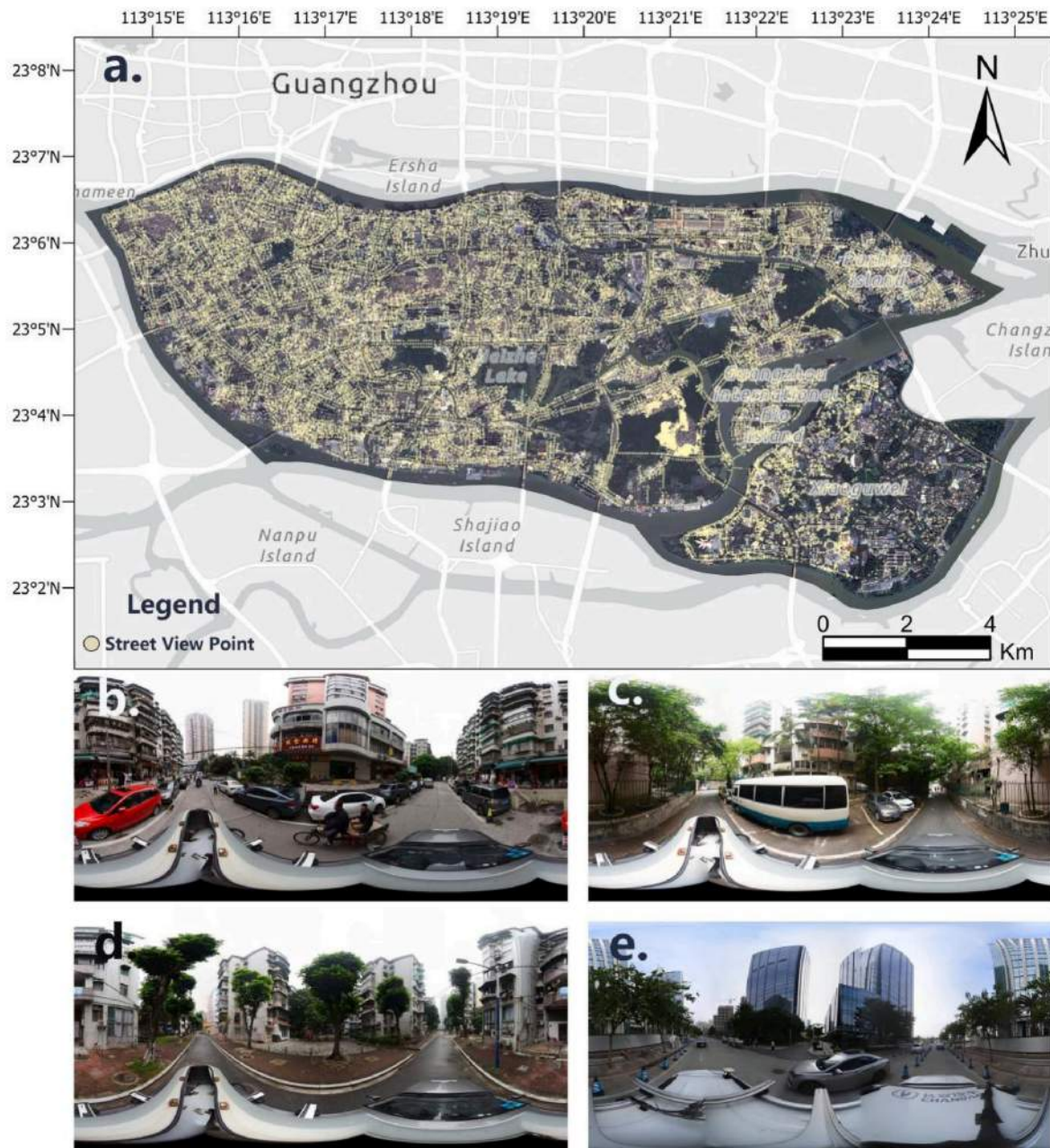


Fig. 5. Distribution of street view sampling points used in this study: (a) Distribution of street view points; (b), (c), (d) and (e) Examples of panoramic Baidu street view crawling results.

visual composition indicators were spatially linked to nearby buildings using buffer-based spatial joins, enabling further analysis at the building level. Fig. 7 provides visual examples of the semantic segmentation results and component extraction.

(3) Deriving visual obstruction metrics from street view composition

Based on the semantic segmentation results, each sampled street-view image was analyzed to quantify three key visual components: sky, vegetation, and buildings. The proportion of pixels belonging to each component was calculated, representing the relative openness and visual enclosure of the local streetscape. Specifically, the sky fraction reflects vertical openness; the vegetation fraction captures the degree of green obstruction from trees and shrubs; and the building fraction quantifies the extent of structural blockage.

To link these visual characteristics with specific buildings, each street view image was spatially associated with its nearest adjacent building. The mean values of the three components across all sampling points surrounding a building were then computed, forming a set of building-level visual obstruction metrics. These metrics were subsequently integrated with the visibility-constrained radiance maps to further refine exposure estimation by accounting for micro-scale barriers not captured by top-down elevation-based analyses.

To quantify the overall obstruction from the source-side view, we formulated an Occlusion Coefficient (O_b). Conceptually, this dimensionless index represents the degree to which street-level features (buildings, vegetation) obstruct light propagation relative to the degree of openness (sky). A higher value indicates greater overall obstruction. The coefficient is calculated by incorporating the three visual factors using a weighted formulation:

$$O_b = \frac{\gamma \cdot SV_v F}{\alpha \cdot SV_b F + \beta \cdot SV_v F + \gamma \cdot SV_s F} \quad (9)$$

where $SV_b F$, $SV_s F$ and $SV_v F$ denote the average fractions of building, sky, and vegetation pixels respectively, calculated from segmented images. The weights α , β , and γ can be adjusted to reflect the relative importance of each visual component in obstructing light transmission.

3.3.3. Construction of the dual-perspective building-scale light exposure index (DBLEI)

Building upon the dual-perspective framework established in Sections 3.3.1 and 3.3.2, we introduce a composite index to quantify nighttime light exposure at the building scale. The receptor-side visibility modeling defines the spatial extent of visible light, capturing view-dependent obstructions from the building's perspective. In parallel, the source-side modeling captures micro-scale attenuation effects arising from the street environment, including partial blockage by trees and adjacent structures.

To integrate these two dimensions of light accessibility, we construct the DBLEI. This index adjusts the total radiance received within each building's visible field by incorporating a street-view-based occlusion coefficient. Specifically, DBLEI is defined as:

$$DBLEI = VCB \times O_b \quad (10)$$

where VCB represents the **total radiance** computed within each building's composite visibility mask (see Equation (8)), and O_b is the **occlusion adjustment factor** derived from the relative proportions of sky, vegetation, and building components in the surrounding street view imagery (see Equation (9)).

The DBLEI formulation allows for flexibility in the selection of the radiance input VCB , enabling the index to be tailored to different analytical purposes. For instance, if VCB is derived from the panchromatic band, the resulting DBLEI reflects general light intensity exposure. Alternatively, if blue-band radiance or the RBLI is used, DBLEI emphasizes exposure to short-wavelength illumination, which is more relevant

to circadian rhythm disruption and public health concerns. This modularity allows the DBLEI to serve both as a general-purpose exposure indicator and as a health-sensitive risk proxy, depending on the wavelength composition of the radiance layer applied.

The DBLEI reflects both the luminous intensity observable from the building and the degree to which the surrounding environment modulates that intensity before reaching the observer. As such, it provides a more realistic and spatially nuanced estimation of light exposure risk, particularly in dense urban settings where structural and vegetative shielding can vary considerably across buildings.

It is important to note that the DBLEI is sensitive to variations in building height. The influence of a building's height is primarily captured through the receptor-side viewshed analysis. Observation points on a taller building are situated at a higher elevation, allowing them to overcome immediate ground-level obstructions and fundamentally alter the visibility field compared to a shorter building at the same location. This altered viewshed captures a different set of environmental features: it can incorporate more distant light sources, but it can also be occluded by other distant features, such as tall buildings or dense tree canopies, that were not in the line-of-sight of the shorter building. Therefore, the resulting Visibility-Constrained Brightness (VCB) value, and consequently the final DBLEI, is a complex function of the specific 3D arrangement of light sources and occluders within this height-dependent viewshed. Thus, the framework is designed to reflect how a building's vertical dimension modulates its potential light exposure.

3.4. Model validation

To evaluate the accuracy and reliability of the proposed DBLEI, ground-based measurements were conducted using a Sky Quality Meter (SQM)—a widely used instrument in astronomical observations and light pollution studies (Cinzano, 2005). The SQM measures sky brightness in units of magnitude per square arcsecond ($\text{mag}/\text{arcsec}^2$), where higher values indicate darker skies and lower levels of light pollution (Teikari, 2007).

In this study, ten validation points were selected within the study area to conduct field measurements. Considering that the overpass time of the SDGSAT-1 satellite over China is approximately 21:30 Beijing time (Liu et al., 2024), and that the satellite's revisit period is not strictly fixed, we scheduled SQM measurements at 21:35 to ensure temporal consistency and maximize the relevance of the comparison.

Following the conversion method proposed by Katz and Levin (2016), the SQM readings were transformed into total radiance values per unit area. A 500-m buffer zone was established around each validation point, and the average building-level exposure index within this zone was extracted. An ordinary least squares (OLS) regression was then performed between the transformed SQM values and the modeled exposure index (Fig. 11) to assess the model's accuracy and reliability.

3.5. Population exposure mapping and health risk zoning

While the DBLEI quantifies potential light exposure, the actual health risk is realized only where high exposure coincides with human presence. To bridge this gap, we integrated the DBLEI with a high-resolution nighttime population surface derived from Baidu Heatmap data. This population-aware approach allows for the identification of critical exposure hotspots. The methodology involved two main steps: (1) processing proxy population data from heatmaps, and (2) performing a spatial integration of the DBLEI and population data to delineate risk zones.

(1) Proxy population data processing based on Baidu heatmaps

Baidu Heatmap data has been widely validated in urban studies as a reasonable proxy for dynamic population distribution estimation (e.g.,

Bao et al., 2023; Zhang et al., 2025). Based on this, we utilized the high spatiotemporal resolution and broad urban coverage of Baidu Heatmap data to collect hourly activity intensity "slices" associated with user location signals.

To align exposure estimates with satellite imagery, we selected heatmap data captured at 21:00 on the same date as the SDGSAT-1 overpass, ensuring temporal consistency. The raw data were supplied in point-based vector format, each feature containing a relative intensity value. We interpolated these points using inverse distance weighting (IDW) to generate a continuous population surface, followed by resampling and spatial clipping to align with our building footprint extents. Pixel values were then normalized to a 0–1 scale, enhancing comparability across areas. The final result is a high-resolution raster

surface representing relative nighttime human activity intensity, which serves as the basis for building-level exposure computation.

(2) Spatial integration of DBLEI and population to estimate exposure risk

To better understand how population density and light exposure interact across urban space, we further assessed their spatial co-distribution using bivariate local Moran's I analysis (Song et al., 2020). While DBLEI and population data provide complementary insights when overlaid, their spatial correlation may vary by neighborhood and density context. This method identifies statistically significant clusters where high or low values of one variable (e.g., population)

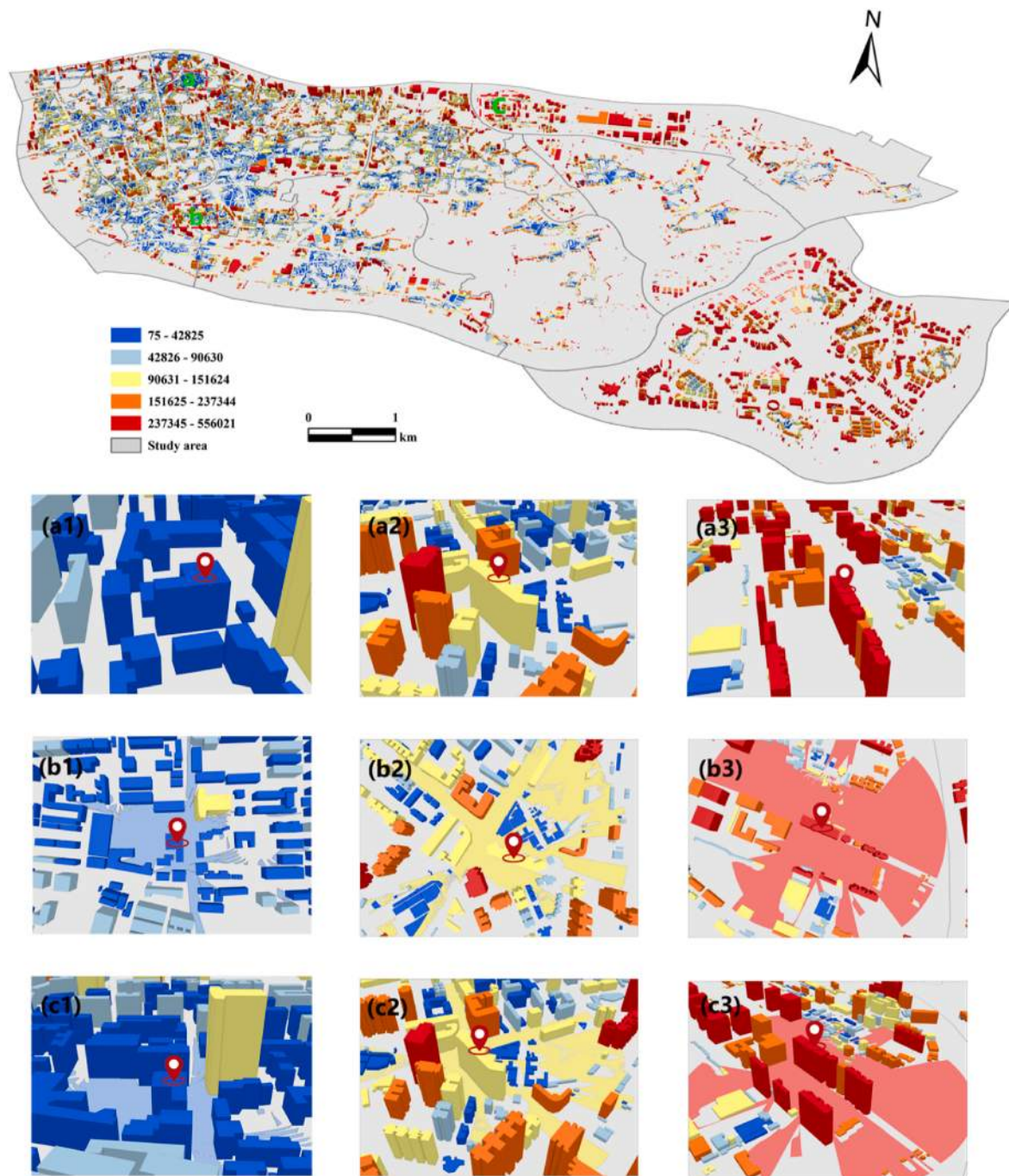


Fig. 6. Spatial distribution of building visibility based on viewshed analysis. (a1–c3) show 3D examples of buildings with low (a1–c1), moderate (a2–c2), and high (a3–c3) visibility ranges, demonstrating the influence of urban form on line-of-sight obstruction.

spatially associate with high or low values of another variable (e.g., DBLEI), revealing potential exposure hotspots where lighting intensity and population aggregation overlap.

The bivariate local Moran's I statistic for each spatial unit iii is computed as:

$$I_i = z_{x,i} \sum_j w_{ij} z_{y,j} \quad (11)$$

where $z_{x,i}$ and $z_{y,j}$ are standardized scores of population density and DBLEI at locations i and j , and w_{ij} is the spatial weight matrix. This spatial statistical approach categorizes local clusters into four types: high-high (HH), low-low (LL), high-low (HL), and low-high (LH). Among them, HH clusters represent areas with both high DBLEI and dense population, and were interpreted as key nighttime light exposure hotspots.

4. Results

4.1. Dual-perspective analysis of urban nighttime light visibility

4.1.1. Receptor-side visibility analysis at the building scale

The receptor-side viewshed analysis revealed pronounced spatial heterogeneity in building-level visibility, with individual visibility fields ranging from 75 to 556,021 m² across the study area (Fig. 6). Buildings located in more open environments—such as along major thoroughfares, intersections, or adjacent to open squares—generally exhibited broader viewsheds, while those situated within dense urban blocks or narrow alleyways were more heavily occluded by surrounding structures. The visible spatial range for individual buildings varied significantly, with some having unobstructed fields of view spanning several hundred meters, while others were limited to a few meters due to close-proximity obstructions.

To illustrate these differences more clearly, several representative buildings were selected from areas with low, moderate, and high visibility ranges. To illustrate these differences more clearly, several representative buildings were selected from areas with low, moderate, and high visibility ranges (Fig. 6 (a1–c3)). In low-density neighborhoods such as Guangzhou Higher Education Mega Center in the southeast of the study area, exhibited the highest visibility levels. This area features a concentration of ten universities, with relatively low building density and wide road corridors, both of which contribute to expansive building viewsheds. In contrast, urban village areas such as WuFengCun, RuiBaoCun, and KangLeCun are characterized by extremely high building density, narrow alleys, and irregular, closely packed residential structures. These morphological conditions result in severely restricted visibility, as demonstrated by the compressed viewsheds and heavy occlusion patterns. The disparity between these contrasting urban forms highlights how street-level openness and building arrangement jointly shape the potential for nighttime light to reach building facades.

When visibility was aggregated at the street level (Table 2), Xiaoguwai Street exhibited the highest average building viewshed area (171,645.4 m²), reflecting its low building density and wide spatial openness. Huazhou Street (103,228.4 m²) and Nanzhou Street also ranked highly, with the latter recording the largest total viewshed area (269,375,328 m²) due to its extensive street length and mixed-use urban form. In contrast, streets such as Sushe (49,231.7 m²), Nanhua West, and Longfeng displayed the lowest average visibility levels, consistent with their compact, high-density urban village morphology. These patterns align with known variations in building typology and spatial layout.

Building on the visibility-based analysis, the cumulative nighttime light radiance received within each building's visible domain was further aggregated to the street level, enabling a more comprehensive understanding of how urban morphology influences light exposure from a radiometric perspective (Table 2). In terms of total radiance within

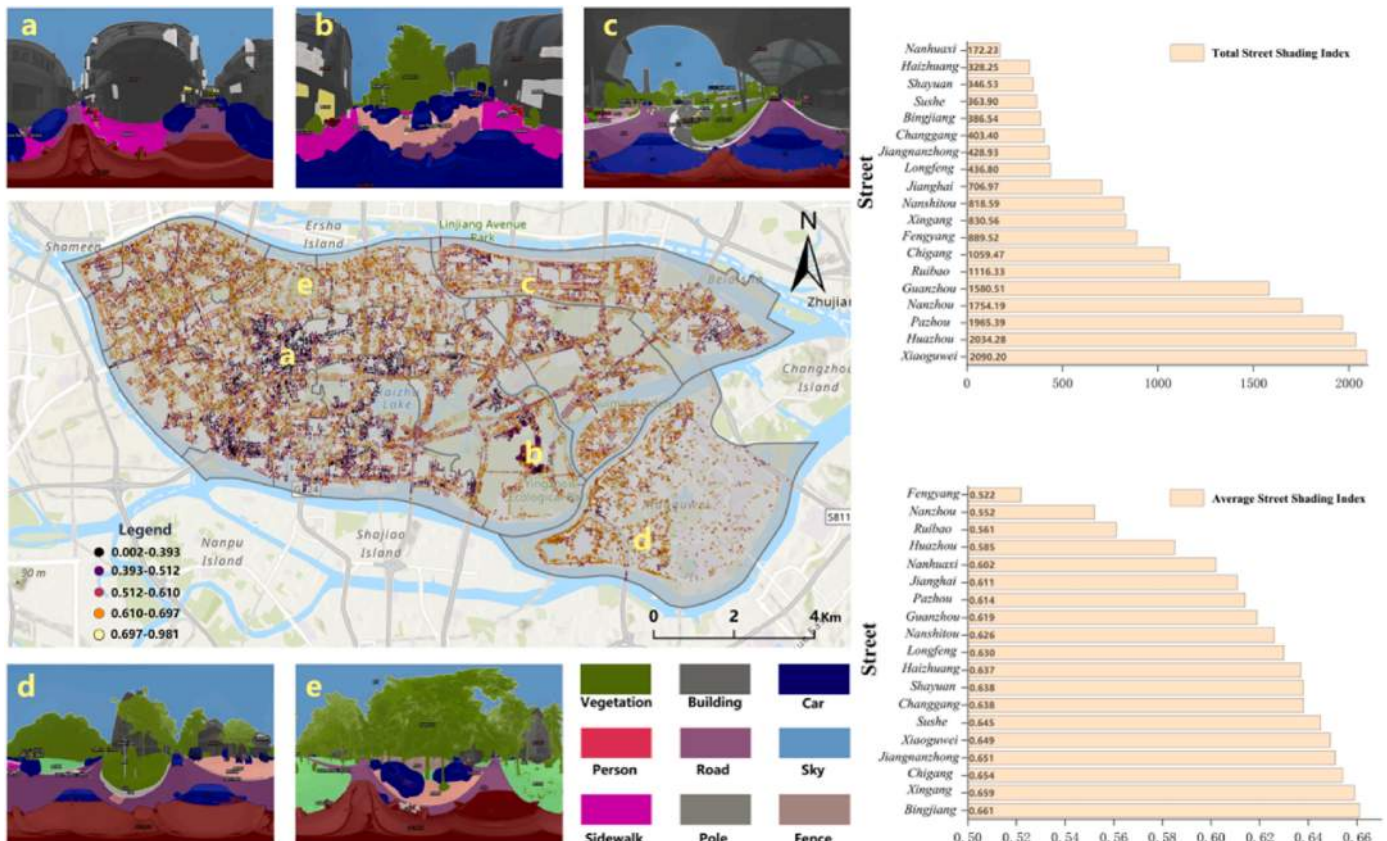


Fig. 7. Street-view-based occlusion gradient map and semantic segmentation examples across different occlusion levels.

Table 2
Average and total visibility and associated radiance values for street-facing buildings in each block.

Street	Average viewshed value (m ²)	Total viewshed value (m ²)	Average Radiance in View (nW·cm ⁻² ·sr ⁻¹)	Total Radiance in View (nW·cm ⁻² ·sr ⁻¹)
Longfeng Street	67706.336	53420300	9121.057	7141787
Nanhuaxi Street	83797.602	2589346	16605.27	5081213
Haizhuang Street	80875.602	45209464	14972.8	8294931
Sushe Street	49231.703	29194400	5030.941	2973287
Jiangnanzhong Street	62439.098	42396148	8458.251	5709320
Shayuan Street	63129.543	35100024	12388.62	6875683
Binjiang Street	68034.695	31908272	19209.13	9009080
Changgang Street	75290.023	51197216	8155.522	5545756
Nanshitou Street	76737.375	97379728	6968.858	8822574
Xingang Street	86646.672	81447872	5344.935	5002859
Ruibao Street	54517.504	131659768	6290.738	15060030
Fengyang Street	61332.188	110581936	5428.137	9743506
Nanzhou Street	75223.492	269375328	4568.894	16297240
Huazhou Street	103228.375	210379424	3202.545	6513977
Chigang Street	93854.664	119946256	15202.55	5545756
Pazhou Street	132660.438	210134128	12806.64	20234480
Jianghai Street	85609.016	101703512	5309.826	6281524
Guanzhou Street	110863.461	197558688	6051.521	10747500
Xiaoguwei Street	171645.406	368179392	7444.658	15968790

building viewsheds, Pazhou Street recorded the highest cumulative value, reaching 20,234,480 nW cm⁻²·sr⁻¹, whereas Sushe Street showed the lowest total value at 2,973,287 nW cm⁻²·sr⁻¹. However, when examining average radiance per building, a different pattern emerged: Binjiang Street exhibited the highest average radiance (19,209.13 nW cm⁻²·sr⁻¹), while Huazhou Street had the lowest (3202.55 nW cm⁻²·sr⁻¹). These findings suggest that both the scale of spatial openness and the intensity of surrounding light sources contribute jointly to shaping the light exposure experienced by individual buildings.

Overall, the analysis underscores the necessity of accounting for receptor-side occlusion in urban lighting exposure assessment, as visibility fundamentally constrains whether artificial light can reach a building's facade.

4.1.2. Source-side openness and obstruction assessment from street view imagery

Although the preceding viewshed analysis captures visibility features from the building's perspective under 3D urban morphology and enables estimation of the light radiance each building receives within its visible domain, it does not account for smaller-scale obstructions directly in front of buildings, such as street trees, fences, or signage, which may significantly attenuate incident light. To address this limitation, we incorporated street-view imagery as a complementary data source to identify and quantify near-ground obstructions that are often invisible in elevation-based models. By performing semantic segmentation on street-level photos, we assessed the relative proportions of key occluding elements (vegetation, buildings, and sky) and examined their spatial variation across different street environments.

Based on the methodology described above, we calculated the occlusion coefficients for 29,174 street-view sampling points across the study area and generated a spatial gradient map to visualize variations in street-level obstruction intensity, where different colors of each street-view point represent the magnitude of occlusion degree—darker colors (with smaller values) indicate that the location is more open. As illustrated in Fig. 7(a–e), examples of semantic segmentation under different occlusion levels show that elements such as vegetation, signage, and lamp posts significantly interfere with ground-level nighttime illumination. These obstructions contribute to noticeable spatial heterogeneity in upward light exposure at the base of buildings.

To further quantify this effect at the street scale, we aggregated the occlusion data to compute the total and average occlusion indices for each street. The total occlusion index displayed a clear three-tier gradient: streets with high overall occlusion (e.g., Nanhuaxi, Haizhuang) ranged from 172.23 to 706.97, while moderately occluded streets (e.g., Nanshitou, Xingang) ranged from 818.59 to 1116.33. In

contrast, low-occlusion streets (e.g., Guanzhou, Nanzhou) exhibited values between 1580.51 and 2090.20, suggesting relatively open spatial configurations.

Although the average occlusion indices across most streets were relatively consistent, Fengyang Street showed a notably lower value (0.522). In contrast, Bingjiang Street recorded the highest average occlusion index (0.661). This pattern may be attributed to the dense and uniform building layout, which results in more consistent mutual obstruction but limited vertical variability—leading to strong average shading effects without a proportional increase in the total occlusion index.

The spatial distribution of the occlusion gradient map reveals a clear pattern of clustering: high-occlusion and low-occlusion points tend to form spatially coherent regions, while medium-occlusion points often appear between them as transitional zones, exhibiting smooth gradient shifts. This spatial structure highlights the varying influence of street-level environmental elements on light propagation across different urban areas.

4.2. Spatial distribution of the dual-perspective Building Light Exposure Index (DBLEI)

4.2.1. DBLEI based on panchromatic exposure

As the baseline representation of general light exposure, the **panchromatic-based DBLEI** was computed to assess overall nighttime illumination levels across urban buildings. As shown in Fig. 8, the distribution of building light exposure exhibits a concentric pattern characterized by lower exposure levels in the central street corridors and higher values in surrounding areas. This suggests that buildings located closest to the street center tend to receive less cumulative radiance due to occlusion or limited angular exposure, while those positioned slightly farther back along the street edges experience greater light exposure.

High exposure levels are observed in areas such as Longfeng Street, Chigang Street, the western part of Pazhou Street, and the central part of Ruibao Street. These locations are characterized by dense building layouts and concentrated artificial lighting, especially near commercial zones and transportation hubs where nighttime illumination is both more abundant and more intense. In contrast, Huazhou Street and Guanzhou Street exhibit relatively low exposure indices. These areas contain large public spaces, fewer buildings, and extensive vegetation coverage, resulting in more open urban forms, sparse light sources, and lower nighttime brightness. Consequently, the buildings in these regions are less exposed to artificial lighting.

To further investigate street-level variation in nighttime light exposure, we conducted a comprehensive analysis of street-facing buildings

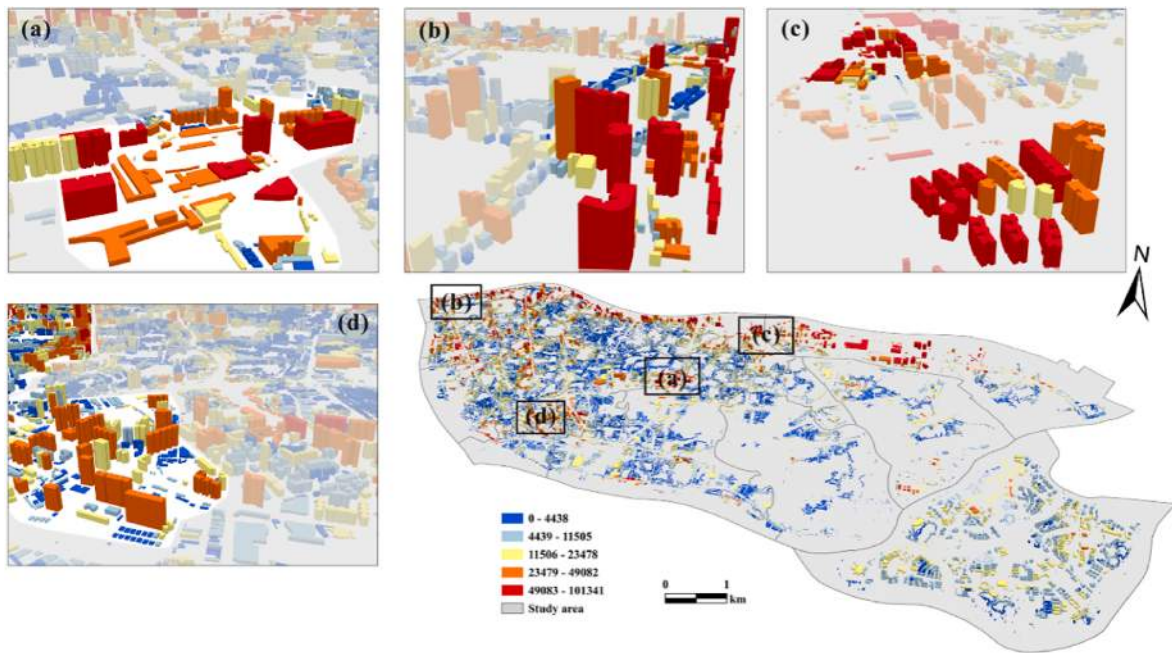


Fig. 8. Spatial distribution of the panchromatic-based Dual-Perspective Building Light Exposure Index (DBLEI). Warmer colors represent higher exposure levels. Subplots (a–d) show detailed examples from selected neighborhoods.

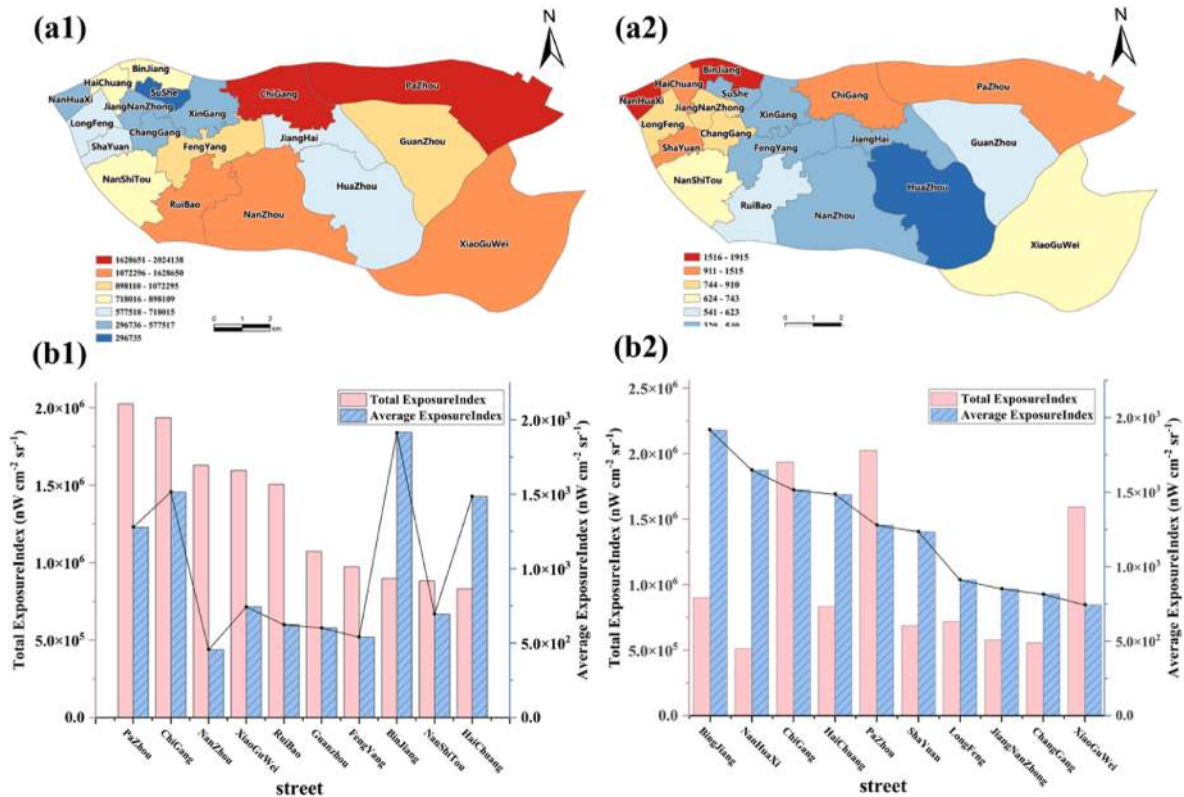


Fig. 9. Spatial distribution and ranking of panchromatic-based DBLEI across streets in the study area. (a1) Total panchromatic-based DBLEI by street; (a2) Average panchromatic-based DBLEI by street; (b1) Top 10 streets ranked by total panchromatic-based DBLEI; (b2) Top 10 streets ranked by average panchromatic-based DBLEI.

across different blocks in the study area. Specifically, we identified the top 10 streets based on both the total panchromatic-based DBLEI (Fig. 9 (b1)) and average DBLEI (Fig. 9 (b2)). Among them, Pazhou Street showed the highest cumulative exposure value, reaching 2,024,138.4

$\text{nW cm}^{-2}\cdot\text{sr}^{-1}$, with an average exposure of 1277.9 $\text{nW cm}^{-2}\cdot\text{sr}^{-1}$. Similarly, Chigang Street recorded a total exposure of 1,935,792.2 $\text{nW cm}^{-2}\cdot\text{sr}^{-1}$ and an average of 1514.7 $\text{nW cm}^{-2}\cdot\text{sr}^{-1}$, indicating substantial nighttime light pollution in both areas.

Fig. 9 (a1–a2) present the spatial distribution of DBLEI at the street level. Notably, blocks such as Binjiang and Nanhua West exhibit relatively high average exposure values but comparatively low total exposure, suggesting that although the building scale may be smaller, the per-building lighting intensity remains significant. This pattern indicates a potentially high degree of light pollution risk, highlighting the need for improved lighting design and mitigation strategies in these residential environments.

4.2.2. DBLEI based on blue-light exposure

In addition to general lighting exposure, we further computed a **blue-light-based DBLEI**, which targets short-wavelength illumination known for its heightened physiological effects due to higher melanopic sensitivity (Silvani et al., 2022). The calculation procedure mirrored that of the panchromatic DBLEI, with the RBLI used as the radiance input. This version of DBLEI emphasizes areas where blue light may pose greater risks to circadian regulation and sleep-related health outcomes.

Fig. 10 (a and b) display the spatial distributions of DBLEI derived from blue-band and panchromatic radiance, respectively, across the study area. These maps reveal visually distinct patterns in exposure levels, especially when comparing the compactness and concentration of high-exposure clusters. The results reveal notable similarities in the low–low clusters of blue-light and panchromatic DBLEI, primarily located in low-density residential zones or open green spaces. However, clear differences emerge in the high–high clusters, where blue-light exposure shows more compact and functionally driven spatial patterns (Fig. 10 (c and d)). These clusters predominantly occur in street-facing buildings located within zones characterized by intensive nighttime functions and distinct land-use typologies (Chen et al., 2023).

High–high clusters of blue-light DBLEI were observed in several functionally dense subareas, including residential districts (e.g., Poly Garden), industrial zones (e.g., Nanji Industrial Park, Yuelong Industrial

Estate), educational campuses (e.g., Sun Yat-sen University, Guangdong Light Industry Vocational and Technical University), and mixed-use commercial–residential areas (e.g., Chigang, Lijiao). These environments share three characteristics: a high density of street-facing buildings, strong and persistent demand for nighttime illumination, and widespread use of high-brightness LED lighting, a dominant source of short-wavelength radiation (Wang et al., 2024).

Furthermore, secondary sources such as advertising light boxes, commercial signage, and reflections from glass curtain walls amplify blue-light exposure by scattering and intensifying lateral illumination. In pedestrian-heavy areas like commercial and university districts, buildings tend to be lower and less obstructed, enabling more direct contact between lighting sources and building façades. The combined effects of urban morphology, activity intensity, and light source characteristics give rise to compact and consistent high–high clustering in blue-light-based DBLEI.

In contrast, high-exposure clustering in the panchromatic DBLEI is more commonly associated with scenic waterfronts and iconic landmarks, where lighting infrastructure is oriented toward aesthetic enhancement rather than functional illumination. Notable clusters were observed near Guangzhou Tower, the Pearl River Pada Beer Culture and Creative Arts Zone, and Haiyin Park, where decorative lighting, often employing broader-spectrum panchromatic sources, is used to shape visual ambience and promote nighttime leisure activities. These findings emphasize the differing spatial drivers behind blue-light and panchromatic exposures: the former shaped by utilitarian lighting in activity-dense corridors, the latter by landscape-oriented lighting in visually prominent environments.

4.2.3. Accuracy validation of the DBLEI using ground-based SQM measurements

To confirm the reliability of the proposed model, the DBLEI was

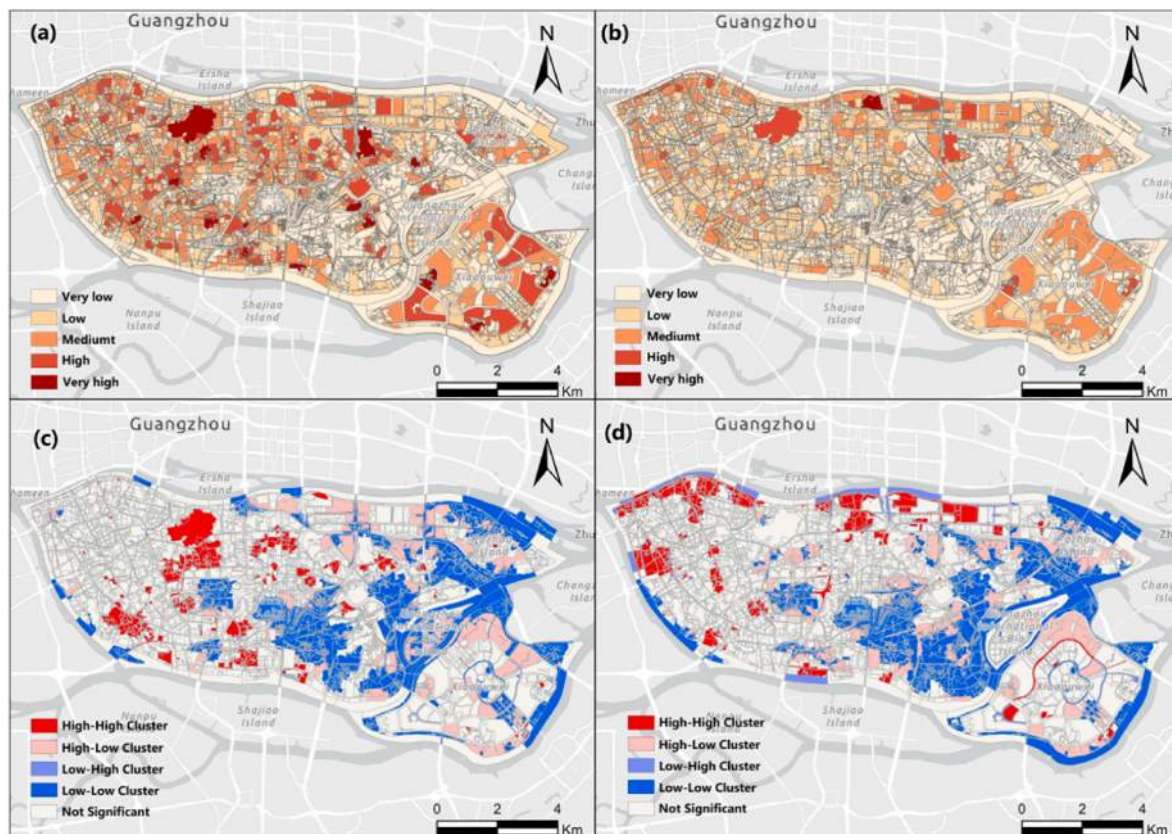


Fig. 10. Spatial distribution (a, b) and local Moran's I clustering (c, d) for the blue-light and panchromatic DBLEI. Note: The color classifications for maps (a) and (b) were calculated independently using the natural breaks (Jenks) method.

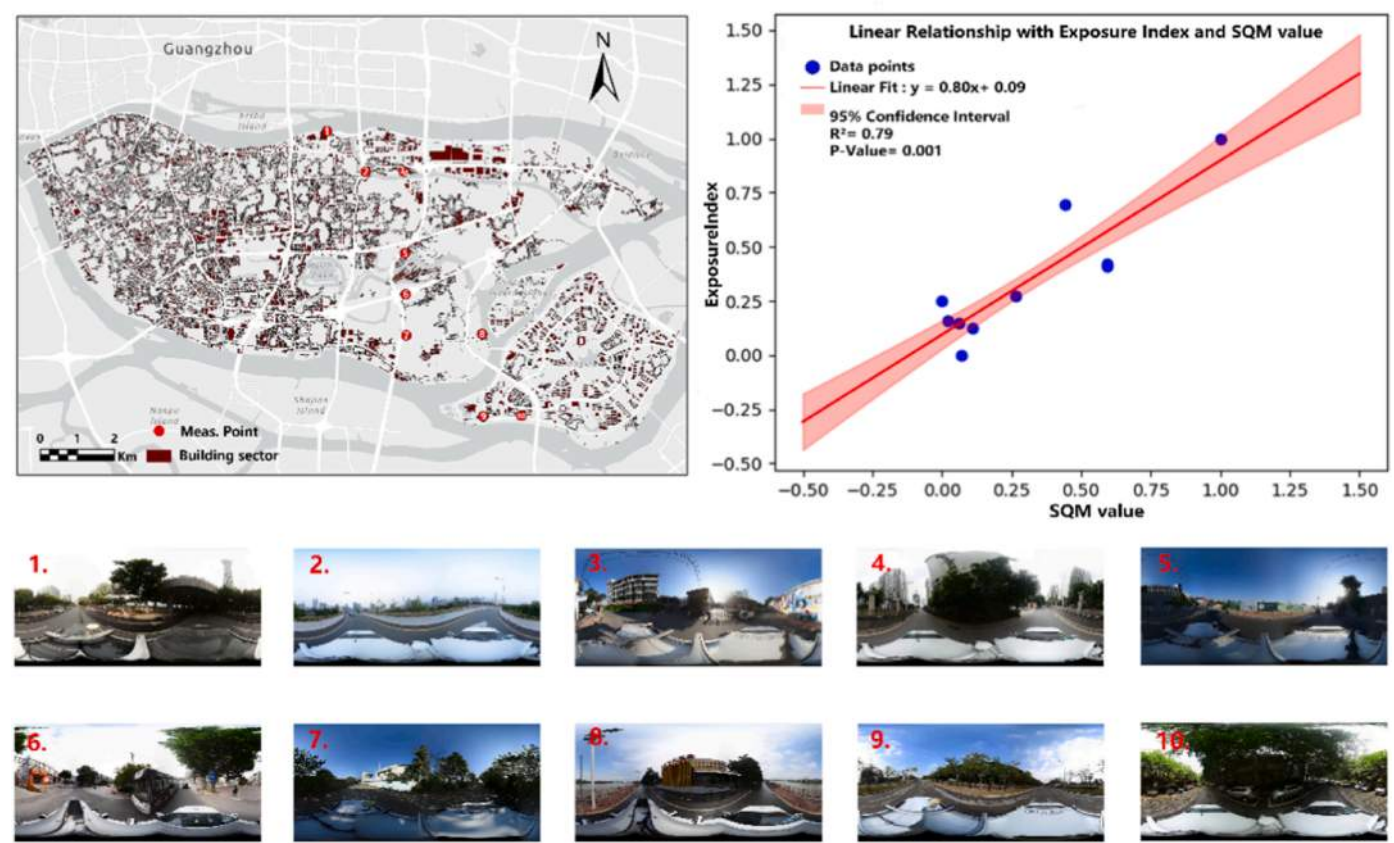


Fig. 11. Validation of the DBLEI using SQM measurements and street-level visual inspections. Note: Left panel: spatial distribution of measurement points and building sectors; Top-right panel: regression between DBLEI and SQM brightness; Bottom-right panel: street-view samples (1–10) at measurement locations.

validated against ground-based SQM measurements. The analysis revealed a strong and statistically significant correlation between the modeled exposure and the ground-truthed data, with a coefficient of determination (R^2) of 0.79 ($p = 0.001$), supporting the model's applicability in complex urban environments (Fig. 11).

4.3. Population-aware identification of nighttime light exposure risk

To translate potential building-level exposure into tangible human health risk, the spatial relationship between the DBLEI and nighttime population density was analyzed. This population-aware assessment identifies critical hotspots where high illumination levels and dense

human activity coincide, revealing areas with the greatest potential for light-related health impacts.

From the bivariate localized Moran index result plots in Fig. 12, the relationship between the blue light exposure suffered by street-front buildings and the accumulation of population can be clearly seen. Firstly, the blue light exposure suffered by street-fronting buildings is more prominently associated with high and high clustered areas of population (Fig. 12 (a)) than panchromatic light exposure (Fig. 12 (b)), suggesting that blue light exposure is closely associated with crowd accumulation, especially in high-density urban areas where the spatial clustering effect between blue light exposure and population distribution is stronger.

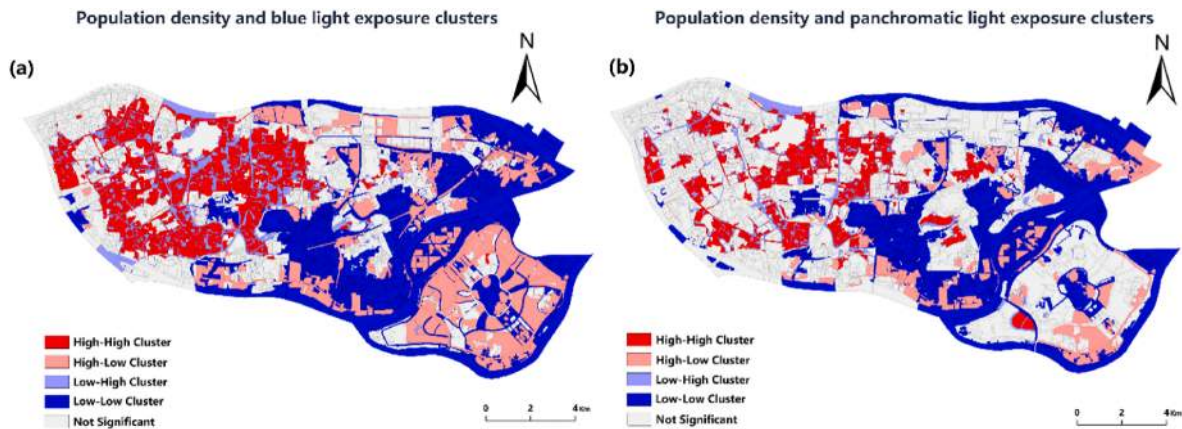


Fig. 12. Bivariate local Moran's I clusters between population distribution and building light exposure. (a) Spatial clusters between population density and blue light exposure; (b) Spatial clusters between population density and panchromatic light exposure.

In addition, low-low clusters with smaller populations and fewer buildings exposed to blue light are mainly distributed in various park areas. Parks are usually open spaces with fewer and relatively lower buildings, and the demand for lighting for crowd activities at night is lower, so lighting facilities are used less, resulting in lower blue light exposure, and the population density in the area is lower, forming a spatial distribution pattern of low-low clusters.

In contrast, in the university town area, although the buildings were exposed to higher blue light, the population density in the area was lower, showing high-low clusters. This phenomenon may be closely related to the functional attributes and structural characteristics of university towns (Dober, 2000), where a large number of educational facilities and open spaces, especially commercial and public areas around the campus, often use strong light sources, leading to increased blue light exposure. Despite the lower population density in the area, the lower height and looser distribution of street-fronting buildings and the weaker shading effect between street-fronting buildings allowed blue light to reach the building facades more widely, which in turn resulted in a high-low cluster pattern of blue light exposure.

These results further demonstrate the significant spatial correlation between blue light exposure and crowd activity and agglomeration, especially in high-density urban areas, where the concentration of blue light exposure is closely related to the degree of population accumulation.

5. Discussion

5.1. A dual-perspective approach for building light exposure assessment

Recent advancements in nighttime light exposure research have increasingly emphasized the importance of high-resolution spatial modeling. However, most existing approaches rely either on top-down remote sensing data or simplified two-dimensional urban representations, often overlooking the complex interplay between lighting sources and urban morphology. These limitations hinder our understanding of how artificial light interacts with the built environment at the human scale.

To improve granularity, Huang et al. (2025) proposed the Floor-Level Exposure Index (FLEI) and Building-Level Exposure Index (BLEI), offering a novel framework for evaluating light exposure from the perspective of different building floors. Their approach provides an important step toward vertical refinement in light pollution assessment. Nevertheless, it primarily focuses on the receptor-side perspective, and does not explicitly consider whether light sources are visible from a given building surface—a factor heavily influenced by urban occlusions such as surrounding buildings or vegetation.

In response to the limitations of single-perspective models, this study introduces a dual-perspective modeling framework that integrates top-down visibility analysis with bottom-up occlusion estimation derived from semantic segmentation of street-view imagery. This approach simultaneously captures the geometric potential for light reception and the micro-scale environmental barriers that constrain actual exposure, offering a more accurate and realistic evaluation of building-level nighttime light exposure.

By combining macro-level structure with micro-level insight, the framework enables a multi-scale understanding of light pollution formation and propagation. At the macro-scale, it examines how urban lighting systems, street configurations, and land-use intensity influence exposure patterns across large areas (Bennie et al., 2014). At the micro scale, it focuses on the exposure conditions of individual street-facing buildings and their immediate surroundings, which are often shaped by façade orientation, vegetation, and the street canyon effect (Guk and Levin, 2020).

This integrative perspective not only overcomes the limitations of single-scale approaches (Levin et al., 2020), but also facilitates the identification of interactions between localized hotspots and broader

urban lighting trends. It provides a more actionable foundation for developing precise mitigation strategies in urban planning and lighting design, and opens new directions for research into health-oriented and environmentally adaptive lighting interventions.

5.2. Functional road hierarchies and their influence on building light exposure

Understanding how urban form influences light pollution is essential for developing effective mitigation strategies, especially in densely populated cities where artificial lighting is highly concentrated. Among urban structural elements, road network hierarchy plays a pivotal role in shaping the spatial configuration of street-facing buildings and the deployment of lighting infrastructure. However, the relationship between road type and building-scale light exposure remains underexplored, particularly from a dual-perspective framework that incorporates both visibility and occlusion.

To address this gap, we conducted a supplementary analysis examining how different road classifications affect nearby building light exposure. Drawing on established schemes (Cook and Petts, 2023), roads were categorized into five functional types: arterial, secondary, local, unclassified, and special-purpose roads (Fig. 13 (a)). For each type, we constructed a 500-m buffer zone and aggregated the Dual-Perspective Building Light Exposure Index (DBLEI) for buildings within that range (Fig. 13 (b)). This approach allowed us to identify systematic patterns in exposure levels across the urban road network and assess how street functionality interacts with urban morphology—such as building density, street width, and vegetation cover—to mediate light propagation.

The results reveal that secondary roads—often located in mixed-use or commercial districts—exhibited the highest average exposure levels. This can be attributed to dense clusters of street-facing buildings and concentrated lighting infrastructure, including signage and façade lighting. Local roads in residential areas also demonstrated elevated exposure, although to a lesser extent, likely due to narrow streets and low vegetation coverage that allow light to reach building façades more directly.

In contrast, arterial roads, despite their greater width and higher traffic volumes, showed more moderate and evenly distributed exposure. This is likely due to their structured lighting systems, vegetated medians, and wider spatial buffers, which help disperse light and reduce direct spillover (Portnov et al., 2020). Unclassified roads, often situated at the urban fringe or peri-urban zones, displayed heterogeneous exposure patterns due to irregular building distributions and inconsistent lighting arrangements. Special-purpose roads—typically designed for logistics, service access, or cultural corridors—recorded the lowest exposure levels, reflecting sparse development and targeted lighting design.

These findings partially align with previous studies (Fotios et al., 2015) that emphasize road typology as a determinant of perceived brightness. However, unlike studies that rely primarily on pedestrian-level observations or luminance measurements, our dual-perspective framework offers building-scale quantification by integrating remote sensing data and street-level occlusion analysis. This enables a more spatially nuanced interpretation of how road type influences light exposure in real-world settings.

From a policy perspective, the results suggest that urban lighting strategies should be tailored to road function and surrounding building configurations. For instance, secondary roads in commercial districts may require stricter façade lighting regulations to prevent light spillover into adjacent residential areas. Meanwhile, local roads could benefit from shielded or adaptive lighting designs to reduce unnecessary exposure. Such differentiated approaches can help formulate context-aware lighting regulations and guide interventions in areas vulnerable to light pollution.

Nonetheless, this analysis is subject to certain limitations. The

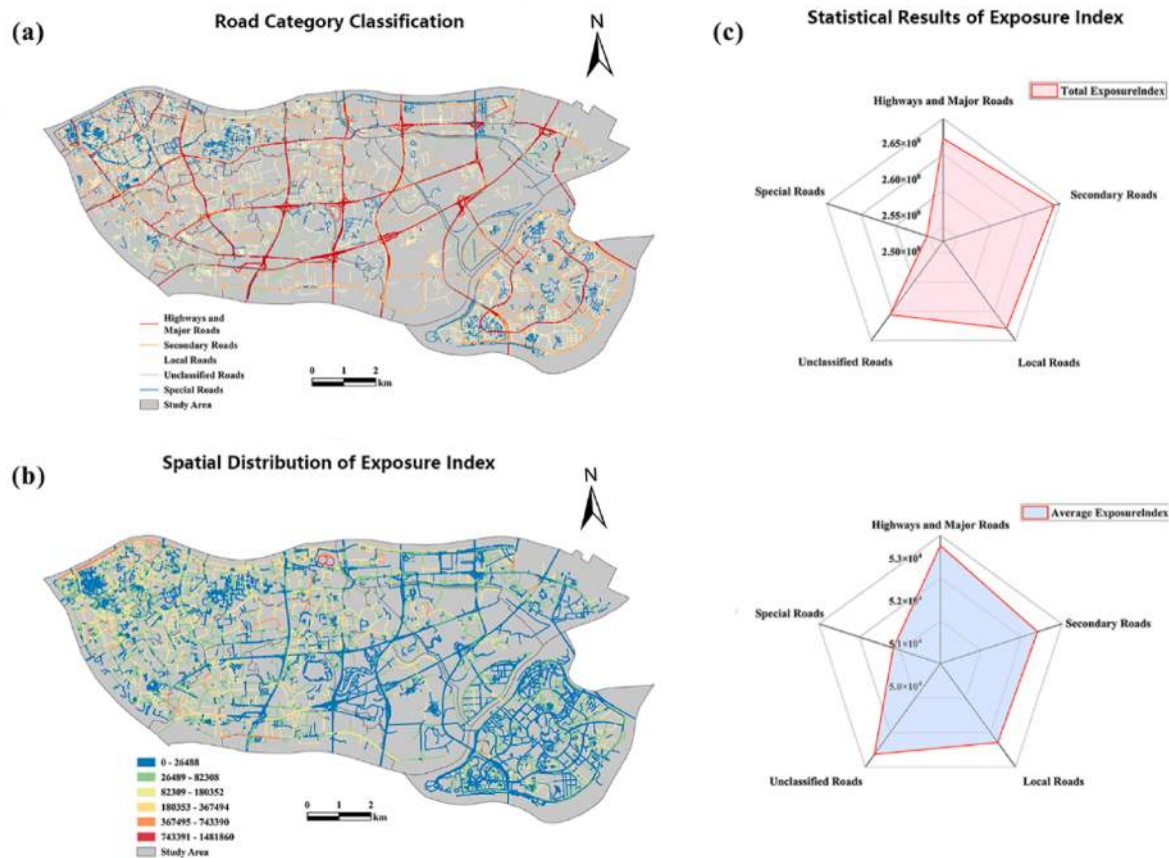


Fig. 13. Analysis of building light exposure across different road hierarchy categories. (a) Classification of roads into five functional categories; (b) Spatial distribution of Exposure Index within 500 m buffers of each road category; (c) Radar plots showing total and average Exposure Index across road types.

classification of roads may not fully capture functional diversity, and the exclusion of dynamic variables—such as real-time lighting intensity, pedestrian flow, and traffic patterns—limits the precision of the exposure modeling. Future research should incorporate these dynamic elements to refine the understanding of how functional street typologies affect nighttime light exposure.

5.3. Policy implications

The findings of this study offer direct, evidence-based guidance for developing tailored urban lighting policies. Our analysis reveals that light exposure is not uniform across the city; rather, it is strongly correlated with road hierarchy and the characteristics of adjacent functional zones. To effectively mitigate light pollution, a one-size-fits-all approach is insufficient. Instead, we propose the following spatially-differentiated strategies:

(1) For Secondary Roads and Commercial Districts.

Our results indicate that secondary roads exhibit the highest average exposure levels, a finding we attribute to dense commercial activity, concentrated signage, and extensive façade lighting. Therefore, policy interventions should be most stringent in these high-risk areas. Following the reviewer's valuable suggestion, specific measures should include: (a) establishing mandatory limits on the blue light ratio for all new and existing LED fixtures to reduce circadian disruption; (b) requiring adaptive dimming systems for commercial signs and digital billboards that automatically reduce brightness after peak business hours; and (c) enforcing stricter regulations on architectural and façade lighting to minimize light trespass and spillover into the night sky and nearby residential properties.

(2) For Local Roads and Residential Areas.

We found that local roads, typically situated in residential zones like Guangzhou University Town, also demonstrate elevated exposure levels, likely due to narrow street canyons that trap light. To protect residents' health and sleep quality, policies in these areas must prioritize mitigation at the source. Recommendations include: (a) promoting the widespread adoption of warm-toned lamps (low Correlated Color Temperature) near sensitive locations such as dormitories and residential buildings; (b) mandating the use of fully shielded luminaires that direct light downward, preventing upward spill; and (c) strategically integrating green infrastructure, such as planting street trees to create vegetating buffers between different functional areas (e.g., teaching and residential zones) to absorb and block stray light.

(3) For Arterial Roads.

Our study shows that arterial roads have more moderate and evenly distributed exposure, benefiting from structured lighting design and vegetated medians. These areas represent a model of successful practice. Policy should therefore focus on codifying these effective strategies into official standards for all new major road construction and retrofitting projects, ensuring that principles of wide spatial buffers and the use of green infrastructure are consistently applied.

By tailoring lighting regulations to the specific findings associated with different road types and urban contexts, cities can move towards a more sustainable and healthy nocturnal environment. These targeted interventions, supported by integrated monitoring frameworks and public awareness campaigns, can effectively reduce the negative impacts of light pollution while maintaining the safety and vibrancy of urban life.

5.4. Limitations

Despite proposing a novel multi-scale framework for assessing building-level light exposure, this study has several limitations. First, due to data constraints, the analysis does not include detailed information on internal floor layouts or vertical segmentation of buildings, which limits the ability to distinguish exposure variations across different heights and reduces the accuracy of vertical exposure assessments. Second, while panoramic street-view imagery provides useful insights into local occlusion effects, it lacks a true three-dimensional representation of the built environment, making it difficult to accurately quantify the shading impact of nearby objects, especially those with complex volumes and varying heights, on building facades. Integrating 3D point cloud or LiDAR data in future studies could substantially improve this aspect. Third, the framework was applied and tested only in two urban subareas, Haizhu District and Guangzhou University Town, which may not fully capture the diversity of urban forms and lighting infrastructures found in other cities. As a result, the generalizability of the findings is limited. To address this, future research should conduct comparative analyses across cities with different densities, spatial configurations, and lighting regulations, in order to validate and adapt the framework to a wider range of urban development contexts and to inform more scalable light pollution mitigation strategies.

6. Conclusions

This study makes three primary contributions to the assessment and management of urban light pollution.

First, we introduce an innovative dual-perspective framework and a corresponding building-level index (DBLEI) for assessing urban nighttime light exposure. By uniquely integrating both the "top-down" visibility from a building's perspective and the "bottom-up" occlusion of light sources at the street level, this approach transcends traditional two-dimensional assessments to capture the complex moderating effects of three-dimensional urban morphology on light propagation.

Second, our application of this framework revealed distinct spatial patterns of light exposure, demonstrating that high-risk areas are not randomly distributed but are strongly linked to urban functions and road hierarchies. Critically, we identified a significant spatial mismatch between general illumination and health-relevant blue light exposure, with the highest risks concentrated in densely populated residential and mixed-use zones where human activity and vulnerable lighting infrastructure overlap.

Finally, these findings have critical implications for urban lighting management and public health. The framework provides a robust, data-driven tool for cities to move beyond one-size-fits-all lighting policies and develop targeted, context-aware mitigation strategies. This includes opportunities for regulating the spectral composition of light in sensitive residential areas, optimizing lighting design along different transportation corridors, and informing evidence-based urban planning that proactively considers light pollution as a key factor for creating healthier and more sustainable nocturnal environments.

CRedit authorship contribution statement

Zhenxiang Ling: Writing – original draft, Visualization, Methodology, Investigation, Conceptualization. **Xianxin Meng:** Visualization, Data curation. **Zihao Zheng:** Writing – review & editing, Funding acquisition, Conceptualization. **Zheng Cao:** Visualization, Resources, Conceptualization. **Zhongwen Hu:** Software, Resources. **Benyan Jiang:** Validation. **Guanhua Guo:** Software. **Yingbiao Chen:** Data curation. **Zhifeng Wu:** Writing – review & editing, Supervision, Project administration.

Declaration of generative AI and AI-assisted technologies in the writing process

During the preparation of this work the author(s) used ChatGPT in order to improve the readability and language of the manuscript. After using this tool/service, the author(s) reviewed and edited the content as needed and take(s) full responsibility for the content of the published article.

Fundings

National Natural Science Foundation of China (No. 42401432)
Guangzhou Basic and Applied Basic Research Program (No. 2024A04J3666)

Open Research Fund Program of MNR Key Laboratory for Geo-Environmental Monitoring of Great Bay Area (GEMLab-2024006)

Data availability

The data and code supporting the findings of this study are openly available in the GitHub repository: <https://github.com/NightSensingLab/dual-view-streetlight-exposure-framework>. Further materials can be provided upon reasonable request to the corresponding author.

Declaration of competing interest

The authors declare no conflict of interest.

References

- Aubé, M., Roby, J., Kocifaj, M., 2013. Evaluating potential spectral impacts of various artificial lights on melatonin suppression, photosynthesis, and star visibility. *PLoS One* 8 (7), e67798. <https://doi.org/10.1371/journal.pone.0067798>.
- Bao, W., Gong, A., Zhang, T., Zhao, Y., Li, B., Chen, S., 2023. Mapping population distribution with high spatiotemporal resolution in Beijing using Baidu heat map data. *Remote Sens.* 15 (2), 458. <https://doi.org/10.3390/rs15020458>.
- Bennie, J., Davies, T.W., Duffy, J.P., Inger, R., Gaston, K.J., 2014. Contrasting trends in light pollution across Europe based on satellite observed nighttime lights. *Sci. Rep.* 4 (1), 3789. <https://doi.org/10.1038/srep03789>.
- Bjelajac, D., Đerčan, B., Kovačić, S., 2021. Dark skies and dark screens as a precondition for astronomy tourism and general well-being. *Inf. Technol. Tourism* 23 (1), 19–43. <https://doi.org/10.1007/s40558-020-00189-9>.
- Buniyaadi, A., Sharma, A., Bhardwaj, S.K., Kumar, V., 2025. Saving from the dark side of light at night: differential effects of complete darkness in the first and second half of dimly illuminated nights on sleep and metabolism. *J. Comp. Physiol.* 211, 473–482. <https://doi.org/10.1007/s00359-025-01747-4>.
- Boyes, D.H., Evans, D.M., Fox, R., Parsons, M.S., Pocock, M.J., 2021. Street lighting has detrimental impacts on local insect populations. *Sci. Adv.* 7 (35), eabi8322. <https://doi.org/10.1126/sciadv.abi8322>.
- Chen, F., Wang, L., Wang, N., Guo, H., Chen, C., Ye, C., Dong, Y., Liu, T., Yu, B., 2024. Evaluation of road network power conservation based on SDGSAT-1 glimmer imagery. *Remote Sens. Environ.* 311, 114273. <https://doi.org/10.1016/j.rse.2024.114273>.
- Chen, L.C., Zhu, Y., Papandreou, G., Schroff, F., Adam, H., 2018. Encoder-decoder with atrous separable convolution for semantic image segmentation. In: *Proceedings of the European Conference on Computer Vision. ECCV*, pp. 801–818. <https://doi.org/10.48550/arXiv.1802.02611>.
- Chen, Y., He, C., Guo, W., Zheng, S., Wu, B., 2023. Mapping urban functional areas using multisource remote sensing images and open big data. *IEEE J. Sel. Top. Appl. Earth Obs. Rem. Sens.* 16, 7919–7931. <https://doi.org/10.1109/JSTARS.2023.3308051>.
- Cinzano, P., 2005. Night sky photometry with sky quality meter. *ISTIL Int. Rep.* 9 (1). https://unihedron.com/projects/darksky/sqmreport_v1p4.pdf.
- Cinzano, P., Falchi, F., Elvidge, C.D., 2001a. The first world atlas of the artificial night sky brightness. *Mon. Not. Roy. Astron. Soc.* 328 (3), 689–707. <https://doi.org/10.1046/j.1365-8711.2001.04822.x>.
- Cinzano, P., Falchi, F., Elvidge, C.D., 2001b. Naked-eye star visibility and limiting magnitude mapped from DMSP-OLS satellite data. *Mon. Not. Roy. Astron. Soc.* 323 (1), 34–46. <https://doi.org/10.1046/j.1365-8711.2001.04213.x>.
- Cook, J., Petts, R.C., 2023. *Rural Road Engineering in Developing Countries*. CRC Press.
- Cozens, P.M., Neale, R.H., Whitaker, J., Hillier, D., Graham, M., 2003. A critical review of street lighting, crime and fear of crime in the British city. *Crime Prev. Community Saf. Int. J.* 5, 7–24. <https://doi.org/10.1057/palgrave.cpcs.8140143>.

- Deprato, A., Haldar, P., Navarro, J.F., Harding, B.N., Lacy, P., Maidstone, R., Moitra, S., Palomar-Cros, A., Durrington, H., Kogevinas, M., Moitra, S., Adan, A., 2025. Associations between light at night and mental health: a systematic review and meta-analysis. *Sci. Total Environ.* 974, 179188. <https://doi.org/10.1016/j.scitotenv.2025.179188>.
- Dober, R.P., 2000. *Campus Landscape: Functions, Forms, Features*. John Wiley & Sons, New York.
- Deziel, N.C., Wang, R., Warren, J.L., Dinauer, C., Ogilvie, J., Clark, C.J., Zhong, C., Wiemels, J.L., Morimoto, L., Metayer, C., Ma, X., 2025. Perinatal exposures to ambient fine particulate matter and outdoor artificial light at night and risk of pediatric papillary thyroid cancer. *Environ. Health Perspect.* 133 (5), 057026. <https://doi.org/10.1289/EHP14849>.
- Falchi, F., Cinzano, P., Duriscoe, D., Kyba, C.C., Elvidge, C.D., Baugh, K., Portnov, B.A., Rybnikova, N.A., Furgoni, R., 2016. The new world atlas of artificial night sky brightness. *Sci. Adv.* 2 (6), e1600377. <https://doi.org/10.1126/sciadv.1600377>.
- Falchi, F., Cinzano, P., Elvidge, C.D., Keith, D.M., Haim, A., 2011. Limiting the impact of light pollution on human health, environment and stellar visibility. *J. Environ. Manag.* 92 (10), 2714–2722. <https://doi.org/10.1016/j.jenvman.2011.06.029>.
- Fotios, S., Unwin, J., Farrall, S., 2015. Road lighting and pedestrian reassurance after dark: a review. *Light. Res. Technol.* 47 (4), 449–469. <https://doi.org/10.1177/1477153514524587>.
- Gaston, K.J., Bennie, J., Davies, T.W., Hopkins, J., 2013. The ecological impacts of nighttime light pollution: a mechanistic appraisal. *Biol. Rev.* 88 (4), 912–927. <https://doi.org/10.1111/brv.12036>.
- Gaston, K.J., Gaston, S., Bennie, J., Hopkins, J., 2015. Benefits and costs of artificial nighttime lighting of the environment. *Environ. Rev.* 23 (1), 14–23. <https://doi.org/10.1139/er-2014-0041>.
- Gibson, J., Olivia, S., Boe-Gibson, G., Li, C., 2021. Which night lights data should we use in economics, and where? *J. Dev. Econ.* 149, 102602. <https://doi.org/10.1016/j.jdeveco.2020.102602>.
- Guk, E., Levin, N., 2020. Analyzing spatial variability in night-time lights using a high spatial resolution color Jilin-1 image—Jerusalem as a case study. *ISPRS J. Photogrammetry Remote Sens.* 163, 121–136. <https://doi.org/10.1016/j.isprsjprs.2020.02.016>.
- Guindon, G.E., Murphy, C.A., Milano, M.E., Seggio, J.A., 2024. Turn off that night light! light-at-night as a stressor for adolescents. *Front. Neurosci.* 18, 1451219. <https://doi.org/10.3389/fnins.2024.1451219>.
- Guo, B., Hu, D., Zheng, Q., 2023. Potentiality of SDGSAT-1 glimmer imagery to investigate the spatial variability in nighttime lights. *Int. J. Appl. Earth Obs. Geoinf.* 119, 103313. <https://doi.org/10.1016/j.jag.2023.103313>.
- Heo, J.Y., Kim, K., Fava, M., Mischoulon, D., Papakostas, G.I., Kim, M.J., Kim, D.J., Chang, K.A.J., Oh, Y., Yu, B.H., Jeon, H.J., 2017. Effects of smartphone use with and without blue light at night in healthy adults: a randomized, double-blind, cross-over, placebo-controlled comparison. *J. Psychiatr. Res.* 87, 61–70. <https://doi.org/10.1016/j.jpsychires.2016.12.010>.
- Hölker, F., Wolter, C., Perkin, E.K., Tockner, K., 2010. Light pollution as a biodiversity threat. *Trends Ecol. Evol.* 25 (12), 681–682. <https://doi.org/10.1016/j.tree.2010.09.007>.
- Huang, H., Wu, B., Wang, Y., Yu, B., Huang, H., Zhang, W., 2025. Towards building floor-level nighttime light exposure assessment using SDGSAT-1 GLI data. *ISPRS J. Photogrammetry Remote Sens.* 223, 375–397. <https://doi.org/10.1016/j.isprsjprs.2025.03.018>.
- Huang, Y., Chen, B., 2025. Nighttime light color characteristics and blue light exposure in China based on SDGSAT-1 glimmer image (No. EGU25-5560). *Copernicus Meet.* <https://doi.org/10.5194/egusphere-egu25-5560>.
- International Research Center of Big Data for SDGs, 2022. Handbook of SDGSAT-1 satellite products. <http://124.16.184.48:6008/downloadresource>. (Accessed 5 August 2025).
- Katz, Y., Levin, N., 2016. Quantifying urban light pollution—A comparison between field measurements and EROS-B imagery. *Remote Sens. Environ.* 177, 65–77. <https://doi.org/10.1016/j.rse.2016.02.017>.
- Kyba, C.C., Tong, K.P., Bennie, J., Birriel, I., Birriel, J.J., Cool, A., Danielsen, A., Davies, T.W., Outer, P.N.D., Edwards, W., Ehlert, R., 2015. Worldwide variations in artificial skyglow. *Sci. Rep.* 5 (1), 8409. <https://doi.org/10.1038/srep08409>.
- Kyba, C.C., Kuester, T., Sánchez de Miguel, A., Baugh, K., Jechow, A., Hölker, F., Bennie, J., Elvidge, C.D., Gaston, K.J., Guanter, L., 2017. Artificially lit surface of Earth at night increasing in radiance and extent. *Sci. Adv.* 3 (11), e1701528. <https://doi.org/10.1126/sciadv.1701528>.
- Levin, N., Kyba, C.C., Zhang, Q., Sánchez de Miguel, A., Román, M.O., Li, X., Portnov, B. A., Molthan, A.L., Jechow, A., Miller, S.D., Wang, Z., 2020. Remote sensing of night lights: a review and an outlook for the future. *Remote Sens. Environ.* 237, 111443. <https://doi.org/10.1016/j.rse.2019.111443>.
- Li, D., Xu, F., Chen, Z., Xie, X., Fan, K., Zeng, Z., 2024. Fine simulation of PM2.5 combined with NPP-VIIRS night light remote sensing and mobile monitoring data. *Sci. Total Environ.* 914, 169955. <https://doi.org/10.1016/j.scitotenv.2024.169955>.
- Li, S., Cheng, L., Liu, X., Mao, J., Wu, J., Li, M., 2019. City type-oriented modeling electric power consumption in China using NPP-VIIRS nighttime stable light data. *Energy* 189, 116040. <https://doi.org/10.1016/j.energy.2019.116040>.
- Lin, Z., Jiao, W., Liu, H., Long, T., Liu, Y., Wei, S., He, G., Portnov, B.A., Trop, T., Liu, M., Li, X., 2023. Modelling the public perception of urban public space lighting based on SDGSAT-1 glimmer imagery: a case study in Beijing, China. *Sustain. Cities Soc.* 88, 104272. <https://doi.org/10.1016/j.scs.2022.104272>.
- Liu, S., Zhou, Y., Wang, F., Wang, S., Wang, Z., Wang, Y., Qin, G., Wang, P., Liu, M., Huang, L., 2024. Lighting characteristics of public space in urban functional areas based on SDGSAT-1 glimmer imagery: a case study in Beijing, China. *Remote Sens. Environ.* 306, 114137. <https://doi.org/10.1016/j.rse.2024.114137>.
- Liu, Y., Kwan, M.P., Zheng, Q., Ma, P., 2025. Coupling fine-grained nighttime Earth observation and optimal buffer for mobility-oriented measures of high-quality outdoor nighttime light exposure. *Environ. Pollut.*, 126861. <https://doi.org/10.1016/j.envpol.2025.126861>.
- Longcore, T., Rich, C., 2004. Ecological light pollution. *Front. Ecol. Environ.* 2 (4), 191–198. [https://doi.org/10.1890/1540-9295\(2004\)002\[0191:ELP\]2.0.CO;2](https://doi.org/10.1890/1540-9295(2004)002[0191:ELP]2.0.CO;2).
- Mander, S., Alam, F., Lovreglio, R., Ooi, M., 2023. How to measure light pollution—A systematic review of methods and applications. *Sustain. Cities Soc.* 92, 104465. <https://doi.org/10.1016/j.scs.2023.104465>.
- Mizon, B., 2012. *Light Pollution: Responses and Remedies*, second ed. Springer Science & Business Media, New York.
- Nagai, N., Ayaki, M., Yanagawa, T., Hattori, A., Negishi, K., Mori, T., Nakamura, T.J., Tsubota, K., 2019. Suppression of blue light at night ameliorates metabolic abnormalities by controlling circadian rhythms. *Investig. Ophthalmol. Vis. Sci.* 60 (12), 3786–3793. <https://doi.org/10.1167/iov.19-27195>.
- Nasrollahi, N., Rostami, E., 2023. The impacts of urban canyons morphology on daylight availability and energy consumption of buildings in a hot-summer Mediterranean climate. *Sol. Energy* 266, 112181. <https://doi.org/10.1016/j.solener.2023.112181>.
- Poot, H., Ens, B.J., de Vries, H., Donners, M.A., Wernand, M.R., Marquenie, J.M., 2008. Green light for nocturnally migrating birds. *Ecol. Soc.* 13 (2). <https://www.jstor.org/stable/26267982>.
- Perini, K., Castellari, P., Calbi, M., Prandi, S., Rocciotiello, E., 2024. Fine dust collection capacity of a moss greening system for the building envelope: an experimental approach. *Build. Environ.* 267, 112203. <https://doi.org/10.1016/j.buildenv.2024.112203>.
- Portnov, B.A., Saad, R., Trop, T., Kliger, D., Svehkina, A., 2020. Linking nighttime outdoor lighting attributes to pedestrians' feeling of safety: an interactive survey approach. *PLoS One* 15 (11), e0242172. <https://doi.org/10.1371/journal.pone.0242172>.
- Ren, W., Wang, Z., Dong, Y., Cao, J., Gao, T., Guo, Q., Chen, Y., 2025. Dim blue light at night worsens high-fat diet-induced kidney damage via increasing corticosterone levels and modulating the expression of circadian clock genes. *Ecotoxicol. Environ. Saf.* 289, 117636. <https://doi.org/10.1016/j.ecoenv.2024.117636>.
- Rouse Jr, J.W., Haas, R.H., Schell, J.A., Deering, D.W., 1973. *Monitoring the Vernal Advancement and Retrogradation (Green Wave Effect) of Natural Vegetation*. No. NASA-CR-132982).
- Silvani, M.I., Werder, R., Perret, C., 2022. The influence of blue light on sleep, performance and wellbeing in young adults: a systematic review. *Front. Physiol.* 13, 943108. <https://doi.org/10.3389/fphys.2022.943108>.
- Smith, M., 2009. Time to turn off the lights. *Nature* 457 (7225), 27. <https://doi.org/10.1038/457027a>.
- Song, W., Wang, C., Chen, W., Zhang, X., Li, H., Li, J., 2020. Unlocking the spatial heterogeneous relationship between per capita GDP and nearby air quality using bivariate local indicator of spatial association. *Resour. Conserv. Recycl.* 160, 104880. <https://doi.org/10.1016/j.resconrec.2020.104880>.
- Teikari, P., 2007. *Light Pollution*. Universitat Politècnica de Catalunya, Spain.
- Uddin, M., Huynh, N., 2017. Truck-involved crashes injury severity analysis for different lighting conditions on rural and urban roadways. *Accid. Anal. Prev.* 108, 44–55. <https://doi.org/10.1016/j.aap.2017.08.009>.
- Wang, N., Hu, Y., Li, X.M., Lan, Y., Kang, C., Yan, L., Dou, C., Miao, C., 2024. Enhancing SDGSAT-1 night light images using a panchromatic guidance denoising algorithm. *Int. J. Appl. Earth Obs. Geoinf.* 128, 103748. <https://doi.org/10.1016/j.jag.2024.103748>.
- Zhang, D., Cheng, B., Shi, L., Gao, J., Long, T., Chen, B., Wang, G., 2022. A destriping algorithm for SDGSAT-1 nighttime light images based on anomaly detection and spectral similarity restoration. *Remote Sens.* 14 (21), 5544. <https://doi.org/10.3390/rs14215544>.
- Zhang, J., Chen, J., Zhu, W., Ren, Y., Cui, J., Jin, X., 2024. Impact of urban space on PM2.5 distribution: a multiscale and seasonal study in the Yangtze River Delta urban agglomeration. *J. Environ. Manag.* 363, 121287. <https://doi.org/10.1016/j.jenvman.2024.121287>.
- Zhang, J., Zhao, X., Han, D., 2025. Assessing the impact of COVID-19 on residents' activities using baidu heat map data: from the lockdown era to the post-pandemic era. *International Journal of Digital Earth* 18 (1), 2454381. <https://doi.org/10.1080/17538947.2025.2454381>.
- Zheng, Q., Weng, Q., Wang, K., 2019. Developing a new cross-sensor calibration model for DMSP-OLS and Suomi-NPP VIIRS night-light imageries. *ISPRS J. Photogrammetry Remote Sens.* 153, 36–47. <https://doi.org/10.1016/j.isprsjprs.2019.04.019>.
- Zheng, Z., Wu, Z., Chen, Y., Guo, G., Cao, Z., Yang, Z., Marinello, F., 2021. Africa's protected areas are brightening at night: a long-term light pollution monitor based on nighttime light imagery. *Glob. Environ. Change* 69, 102318. <https://doi.org/10.1016/j.gloenvcha.2021.102318>.